Simulation of three-dimensional free-surface flows using two-dimensional multilayer shallow water equations

Saida Sari[1,*] Thomas Rowan[2,†] Mohammed Seaid[2,‡] Fayssal Benkhaldoun[1,§]

[1] *LAGA, Université Paris 13, 99 Av J.B. Clement, 93430 Villetaneuse, France*
[2] *School of Engineering, University of Durham, South Road, Durham DH1 3LE, UK*

Abstract

We present an efficient and conservative Eulerian-Lagrangian method for solving two-dimensional hydrostatic multilayer shallow water flows with mass exchange between the vertical layers. The method consists of a projection finite volume method for the Eulerian stage and a method of characteristics to approximate the numerical fluxes for the Lagrangian stage. The proposed method is simple to implement, satisfies the conservation property and it can be used for multilayer shallow water equations on non-flat bathymetry including eddy viscosity and Coriolis forces. It offers a novel method of calculating stratified vertical velocities without the use of the Navier-Stokes equations. Numerical results are presented for several examples and the obtained results for a free-surface flow problem are in close agreement with the analytical solutions. We also test the performance of the proposed method for a test example of wind-driven flows with recirculation.

Keywords. Multilayer shallow water equations; incompressible hydrostatic flows; Eulerian-Lagrangian scheme; finite volume solver; projection method.

1 Introduction

Incompressible Navier-Stokes equations have been widely used in the literature to simulate water flows including eddy diffusion and Coriolis forces, see for example [13, 31, 26]. Further references on a general overview of shallow water wave modelling include [19, 21, 18, 20] among others. However, for free-surface flows these models frequently become complicated due to the presence of moving boundaries within the flow domain and also due to the inclusion of hydrostatic pressure. Under certain assumptions these models can be replaced by the well-established shallow water equations. Indeed, the shallow water equations can be derived by depth-averaging the three-dimensional Navier-Stokes equations assuming that the pressure is hydrostatic and the vertical scale is far smaller than the horizontal scale, see [1] among others. In their depth-averaged form, shallow water equations have been used to model many engineering problems in hydraulics and free-surface flows including tides in coastal regions, rivers, reservoir and open channel flows among others, see for instance [23, 12, 14]. However, since these models are depth averaged, the vertical distribution of velocity field is not resolved and the bed friction is expressed only in terms of the mean velocity rather than the velocity near the bottom. Hence, the three-dimensional modeling of the hydrodynamic equations is needed for a better representation of the flow features, especially for recirculation flows and for solution of near-field problems involving sediment transport and thermal discharges in rivers and coastal waters.

Since standard shallow water models have been well developed, attention has been shifted to the shortcomings of this type of modeling namely, the use of single velocity profile for the entire depth of

*sari@math.univ-paris13.fr
†thomas.rowan@durham.ac.uk
‡m.seaid@durham.ac.uk
§fayssal@math.univ-paris13.fr

the fluid. This has been overcame with the recent introduction of multilayer shallow water equations for geophysical flows. Two-layer shallow water equations have been used to model immiscible fluids, see for example [2, 11, 17]. Multilayer shallow water equations with exchange terms have also been investigated in [3, 5, 15, 4] among others. These multilayer models can be derived by using a semi-discretization in the vertical direction of P_0 finite element types for the water velocity in the three-dimensional Navier-Stokes equations. The attractive points of this class of multilayer models include the fact that they avoid the computationally demanding methods required to solve the three-dimensional Navier-Stokes equations and at the same time providing stratified flow velocities as the pressure distribution is hydrostatic. Here, the flow problem can be approximated as a layered system made of multiple shallow fluids of distinct heights but with exchange terms between these layers. These fluids can also differ in terms of density, compressibility, viscosity and potential for mixing among others. During the last decades, multilayer shallow water models have attracted more attention and have been used for numerical simulation of a variety of hydrodynamical flows such as estuaries, bays and other nearshore regions where water flows interact with the bed geometry and wind shear stresses. However, most of these models consider only the one-dimensional version of the multilayer shallow water equations. To the best of our knowledge, simulation of two-dimensional multilayer shallow water equations with exchange terms is presented for the first time.

Developing highly accurate numerical solvers for multilayer shallow water equations presents a challenge due to the nonlinear aspect of these equations and their coupling through the source terms. More precisely, the difficulty in these multilayer models lies from the coupling terms involving some derivatives of the unknown physical variables that make the system nonconservative and eventually non-hyperbolic, see for example [2, 5]. In the case of one-dimensional multilayer models, a class of kinetic schemes have been used in [3, 5] among others. However, the numerical dissipation and the semi-implicit treatment of source terms may limit the performance of these methods. The lattice Boltzmann method has also been applied to the multilayer shallow water equations in [30] but the complexity of this method is significant. A class of Eulerian-Lagrangian methods have also used in [4] to solve the one-dimensional multilayer shallow water equations. This method avoids the solution of Riemann problems and belongs to the finite volume predictor-corrector type methods. The predictor stage uses the method of characteristics to reconstruct the numerical fluxes whereas the corrector stage recovers the conservation equations in the finite volume framework. The proposed method is simple, fast, conservative, well-balanced, non-oscillatory and suitable for multilayer shallow water equations for which Riemann solvers are no available. Numerical comparisons reported in [4] for one-dimensional multilayer shallow water equations demonstrate that this method is robust and more accurate than the kinetic schemes. In the current study, our main objective is to develop a class of numerical methods that are simple, easy to implement, and accurately solves the multilayer shallow water equations in two space dimensions without relying on Riemann solvers. This objective is reached by a projection of the multilayer shallow water system in the local coordinates and a second-order splitting operator for the time integration. To solve the projected system we extend the Eulerian-Lagrangian method studied in [4] to two-dimensional problems. Several numerical examples are presented to verify the performance of the proposed Eulerian-Lagrangian method to accurately solve the two-dimensional multilayer shallow water equations. We demonstrate the model capability of calculating lateral and vertical distributions of velocities for the multilayer shallow water flows over both flat and no-flat beds. The method is also verified against results obtained using the Navier-Stokes equations for a dam-break problem. Numerical results are also presented for a two-dimensional test problem of wind-driven circulation flows.

The outline of the paper is as follows. In section 2, we recall the two-dimensional multilayer shallow water equations. The Eulerian-Lagrangian method for the multilayer shallow water equations is described in section 3. This includes the reconstruction of the numerical fluxes and the discretization of source terms. Numerical results are presented in section 4. We examine the performance of the proposed method for several free-surface flows and comparison to hydrostatic Navier-Stokes simulations is also presented. Conclusions are summarized in section 5.

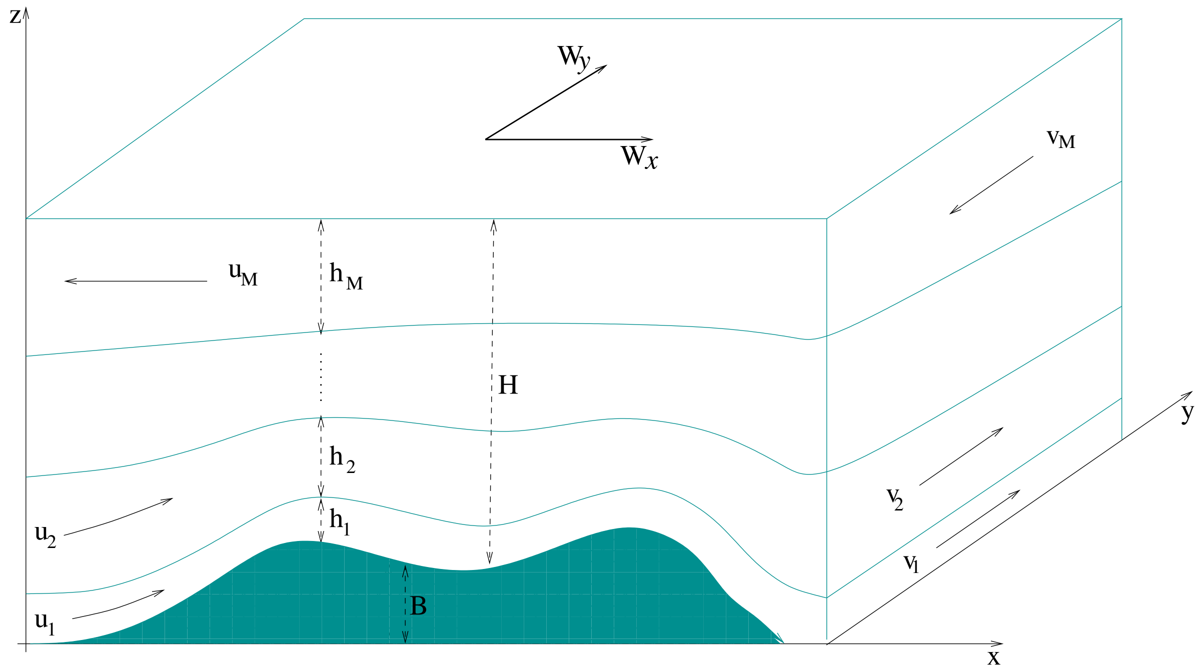

Figure 2.1: Illustration of a two-dimensional multilayer shallow water system on a non-flat topography.

2 Two-dimensional multilayer shallow water equations

Multilayer shallow water equations have been derived from the three-dimensional hydrostatic incompressible Navier-Stokes equations with unknown free-surface by considering the vertical P_0-type discretization of the horizontal velocity. This vertical discretization defines a series of layers in the flow domain and the equations are vertically integrated on each layer separately, compare [6, 3, 5, 15] for more details on the steps used to derive these models. Here, we consider the two-dimensional version of the model written in a conservative form as

$$
\begin{aligned}
\frac{\partial H}{\partial t} + \sum_{\alpha=1}^{M} \frac{\partial}{\partial x}\left(l_\alpha H u_\alpha\right) + \sum_{\alpha=1}^{M} \frac{\partial}{\partial y}\left(l_\alpha H v_\alpha\right) &= 0, \\
\frac{\partial}{\partial t}\left(l_\alpha H u_\alpha\right) + \frac{\partial}{\partial x}\left(l_\alpha H u_\alpha^2 + \frac{1}{2} g l_\alpha H^2\right) + \frac{\partial}{\partial y}\left(H u_\alpha v_\alpha\right) &= -g l_\alpha H \frac{\partial B}{\partial x} + \omega_c l_\alpha H v_\alpha + F_\alpha, \\
\frac{\partial}{\partial t}\left(l_\alpha H v_\alpha\right) + \frac{\partial}{\partial x}\left(H u_\alpha v_\alpha\right) + \frac{\partial}{\partial y}\left(l_\alpha H v_\alpha^2 + \frac{1}{2} g l_\alpha H^2\right) &= -g l_\alpha H \frac{\partial B}{\partial y} - \omega_c l_\alpha H u_\alpha + G_\alpha,
\end{aligned}
\tag{2.1}
$$

where $\mathbf{u}_\alpha = (u_\alpha, v_\alpha)^T$ is the local water velocity for the αth layer, $B(x, y)$ the topography of the basin, g the gravitational acceleration, ω_c is the Coriolis parameter resulting from rotation of the earth, $H(t, x, y)$ denotes the water height of the whole flow system and l_α denotes the relative size of the αth layer with

$$
l_\alpha > 0, \qquad \sum_{\alpha=1}^{M} l_\alpha = 1.
$$

The water height $h_\alpha(t, x, y)$ of the αth layer is defined as

$$
h_\alpha = l_\alpha H, \qquad \alpha = 1, 2, \ldots, M,
$$

where M is the total number of layers in the flow domain, see Figure 2.1 for a simplified illustration of a multilayer shallow water flow system. In (2.1), the source term F_α is the external force in x-direction acting on the αth layer and accounting for the friction and momentum exchange effects. Thus,

$$F_\alpha = \mathcal{F}_\alpha^{(u)} + \mathcal{F}_\alpha^{(\nu)} + \mathcal{F}_\alpha^{(b)} + \mathcal{F}_\alpha^{(w)} + \mathcal{F}_\alpha^{(\mu)}, \qquad \alpha = 1, 2, \dots, M, \tag{2.2}$$

where the first term $\mathcal{F}_\alpha^{(u)}$ is related to the x-momentum exchange between the layers that are defined through the vertical P_0 discretization of the flow domain. The forcing term $\mathcal{F}_\alpha^{(\nu)}$ is due to the horizontal diffusion and the three last terms $\mathcal{F}_\alpha^{(b)}$, $\mathcal{F}_\alpha^{(w)}$ and $\mathcal{F}_\alpha^{(\mu)}$ are related to friction effects. Here, following the techniques presented in [6] the advection term $\mathcal{F}_\alpha^{(u)}$ is given by

$$\mathcal{F}_\alpha^{(u)} = u_{\alpha+1/2}\mathcal{E}_{\alpha+1/2}^x - u_{\alpha-1/2}\mathcal{E}_{\alpha-1/2}^x, \tag{2.3}$$

where the mass exchange terms $\mathcal{E}_{\alpha+1/2}^x$ are computed as

$$\mathcal{E}_{\zeta+1/2}^x = \begin{cases} 0, & \text{if} \quad \zeta = 0, \\ \displaystyle\sum_{\beta=1}^{\zeta} \left(\frac{\partial (h_\beta u_\beta)}{\partial x} - l_\beta \sum_{\gamma=1}^{M} \frac{\partial (h_\gamma u_\gamma)}{\partial x} \right), & \text{if} \quad \zeta = 1, 2, \dots, M-1, \\ 0, & \text{if} \quad \zeta = M, \end{cases} \tag{2.4}$$

and the interface velocity $u_{\alpha+1/2}$ in (2.3) is computed by a simple upwind method using the sign of the mass exchange term *i.e.*

$$u_{\alpha+1/2} = \begin{cases} u_\alpha, & \text{if} \quad \mathcal{E}_{\alpha+1/2}^x \geq 0, \\ u_{\alpha+1}, & \text{if} \quad \mathcal{E}_{\alpha+1/2}^x < 0. \end{cases} \tag{2.5}$$

The vertical kinematic eddy viscosity term $\mathcal{F}_\alpha^{(\mu)}$ takes into account the friction between neighbouring layers and it is defined as

$$\mathcal{F}_\alpha^{(\mu)} = \begin{cases} 2\nu \dfrac{u_2 - u_1}{(l_2 + l_1) H}, & \text{if} \quad \alpha = 1, \\ 2\nu \dfrac{u_{\alpha+1} - u_\alpha}{(l_{\alpha+1} + l_\alpha) H} - 2\nu \dfrac{u_\alpha - u_{\alpha-1}}{(l_\alpha + l_{\alpha-1}) H}, & \text{if} \quad \alpha = 2, 3, \dots, M-1, \\ -2\nu \dfrac{u_M - u_{M-1}}{(l_M + l_{M-1}) H}, & \text{if} \quad \alpha = M, \end{cases} \tag{2.6}$$

where ν is the eddy viscosity. Note that a generalized derivation of the viscous tensor in multilayer shallow water equations has also been reported in [15]. Furthermore, the interface velocity in (2.5) has been approximated as in [15] using the average between the two velocities $u_{\alpha+1}$ and u_α. The external friction terms in (2.2) are given by

$$\mathcal{F}_\alpha^{(b)} = \begin{cases} -\dfrac{\tau_b^x}{\rho}, & \text{if} \quad \alpha = 1, \\ 0, & \text{if} \quad \alpha = 2, 3, \dots, M, \end{cases} \qquad \mathcal{F}_\alpha^{(w)} = \begin{cases} 0, & \text{if} \quad \alpha = 1, 2, \dots, M-1, \\ \dfrac{\tau_w^x}{\rho}, & \text{if} \quad \alpha = M, \end{cases} \tag{2.7}$$

with ρ is the water density, τ_b^x and τ_w^x are respectively, the bed shear stress and the shear of the blowing wind defined by the water velocity (u_1, v_1) and the wind velocity $w = (w_x, w_y)^T$ as

$$\tau_b^x = \rho C_b u_1 \sqrt{u_1^2 + v_1^2}, \qquad \tau_w^x = \rho C_w w_x \sqrt{w_x^2 + w_y^2}, \tag{2.8}$$

where C_b is the bed friction coefficient, which may be either constant or estimated using the Manning equation as

$$C_b = \frac{g n_b^2}{H^{1/3}},$$

where n_b is the Manning roughness coefficient of the bed and the wind friction coefficient C_w is defined as [27]

$$C_w = \frac{\sigma^2 \rho_a}{H},$$

where σ is the wind stress coefficient and ρ_a is the air density. The horizontal diffusion terms $\mathcal{F}_\alpha^{(\nu)}$ in (2.2) are defined as

$$\mathcal{F}_\alpha^{(\nu)} = \nu_H \frac{\partial}{\partial x}\left(l_\alpha H \frac{\partial u_\alpha}{\partial x}\right) + \nu_H \frac{\partial}{\partial y}\left(l_\alpha H \frac{\partial u_\alpha}{\partial y}\right), \qquad \alpha = 1, 2, \ldots, M, \tag{2.9}$$

where ν_H is the horizontal viscosity coefficient.

Similarly, the source term G_α is the external force in y-direction acting on the layer α and accounting for the friction and momentum exchange effects. Thus,

$$G_\alpha = \mathcal{G}_\alpha^{(u)} + \mathcal{G}_\alpha^{(\nu)} + \mathcal{G}_\alpha^{(b)} + \mathcal{G}_\alpha^{(w)} + \mathcal{G}_\alpha^{(\mu)}, \qquad \alpha = 1, 2, \ldots, M, \tag{2.10}$$

where the first term $\mathcal{G}_\alpha^{(u)}$ is related to the y-momentum exchanges between the layers, $\mathcal{G}_\alpha^{(b)}$, $\mathcal{G}_\alpha^{(w)}$ and $\mathcal{G}_\alpha^{(\mu)}$ are related to friction effects. Hence, the advection term $\mathcal{G}_\alpha^{(u)}$ is given by

$$\mathcal{G}_\alpha^{(u)} = v_{\alpha+1/2}\mathcal{E}_{\alpha+1/2}^y - v_{\alpha-1/2}\mathcal{E}_{\alpha-1/2}^y, \tag{2.11}$$

where the mass exchange terms $\mathcal{E}_{\alpha+1/2}^y$ can be computed as

$$\mathcal{E}_{\zeta+1/2}^y = \begin{cases} 0, & \text{if} \quad \zeta = 0, \\ \displaystyle\sum_{\beta=1}^{\zeta}\left(\frac{\partial\left(h_\beta v_\beta\right)}{\partial y} - l_\beta \sum_{\gamma=1}^{M}\frac{\partial\left(h_\gamma v_\gamma\right)}{\partial y}\right), & \text{if} \quad \zeta = 1, 2, \ldots, M-1, \\ 0, & \text{if} \quad \zeta = M, \end{cases} \tag{2.12}$$

and the interface velocity $v_{\alpha+1/2}$ is computed by

$$v_{\alpha+1/2} = \begin{cases} v_\alpha, & \text{if} \quad \mathcal{E}_{\alpha+1/2}^y \geq 0, \\ v_{\alpha+1}, & \text{if} \quad \mathcal{E}_{\alpha+1/2}^y < 0. \end{cases} \tag{2.13}$$

The vertical kinematic eddy viscosity term $\mathcal{G}_\alpha^{(\mu)}$ takes into account the friction between neighboring layers and it is defined as

$$\mathcal{G}_\alpha^{(\mu)} = \begin{cases} 2\nu \dfrac{v_2 - v_1}{\left(l_2 + l_1\right) H}, & \text{if} \quad \alpha = 1, \\ 2\nu \dfrac{v_{\alpha+1} - v_\alpha}{\left(l_{\alpha+1} + l_\alpha\right) H} - 2\nu \dfrac{v_\alpha - v_{\alpha-1}}{\left(l_\alpha + l_{\alpha-1}\right) H}, & \text{if} \quad \alpha = 2, 3, \ldots, M-1, \\ -2\nu \dfrac{v_M - v_{M-1}}{\left(l_M + l_{M-1}\right) H}, & \text{if} \quad \alpha = M. \end{cases} \tag{2.14}$$

The external friction terms are given by

$$\mathcal{G}_\alpha^{(b)} = \begin{cases} -\dfrac{\tau_b^y}{\rho}, & \text{if} \quad \alpha = 1, \\ 0, & \text{if} \quad \alpha = 2, 3, \ldots, M, \end{cases} \qquad \mathcal{G}_\alpha^{(w)} = \begin{cases} 0, & \text{if} \quad \alpha = 1, 2, \ldots, M-1, \\ \dfrac{\tau_w^y}{\rho}, & \text{if} \quad \alpha = M, \end{cases} \tag{2.15}$$

with

$$\tau_b^y = \rho C_b v_1 \sqrt{u_1^2 + v_1^2}, \qquad \tau_w^y = \rho C_w w_y \sqrt{w_x^2 + w_y^2}. \tag{2.16}$$

The horizontal diffusion term $\mathcal{F}_\nu^y$ is defined as

$$\mathcal{F}_\alpha^{(\nu)} = \nu_H \frac{\partial}{\partial x}\left(l_\alpha H \frac{\partial v_\alpha}{\partial x}\right) + \nu_H \frac{\partial}{\partial y}\left(l_\alpha H \frac{\partial v_\alpha}{\partial y}\right), \qquad \alpha = 1, 2, \ldots, M. \tag{2.17}$$

Note that the bed friction forcing terms $\mathcal{F}_\alpha^{(b)}$ and $\mathcal{G}_\alpha^{(b)}$ are acting only on the lower layer, whereas the wind-driven forcing terms $\mathcal{F}_\alpha^{(w)}$ and $\mathcal{G}_\alpha^{(w)}$ are acting only on the upper layer. It should also be stressed that the internal friction terms $\mathcal{F}_\alpha^{(\mu)}$ and $\mathcal{G}_\alpha^{(\mu)}$ model the friction between neighboring layers, see [3] for further details. The equations (2.1) can also be displayed in compact vector form as

$$\frac{\partial \mathbf{W}}{\partial t} + \frac{\partial \mathbf{F}(\mathbf{W})}{\partial x} + \frac{\partial \mathbf{G}(\mathbf{W})}{\partial y} = \mathbf{Q}(\mathbf{W}) + \mathbf{R}(\mathbf{W}), \tag{2.18}$$

where $\mathbf{W}$ is the vector of conserved variables, $\mathbf{F}$ and $\mathbf{G}$ the vectors of flux functions, $\mathbf{Q}$ and $\mathbf{R}$ are the vector of source terms defined by

$$\mathbf{W} = \begin{pmatrix} H \\ l_1 H u_1 \\ l_2 H u_2 \\ \vdots \\ l_M H u_M \\ l_1 H v_1 \\ l_2 H v_2 \\ \vdots \\ l_M H v_M \end{pmatrix}, \quad \mathbf{F}(\mathbf{W}) = \begin{pmatrix} \sum_{\alpha=1}^{M} l_\alpha H u_\alpha \\ l_1 H u_1^2 + \frac{1}{2} g l_1 H^2 \\ l_2 H u_2^2 + \frac{1}{2} g l_2 H^2 \\ \vdots \\ l_M H u_M^2 + \frac{1}{2} g l_M H^2 \\ l_1 H u_1 v_1 \\ l_2 H u_2 v_2 \\ \vdots \\ l_M H u_M v_M \end{pmatrix}, \quad \mathbf{G}(\mathbf{W}) = \begin{pmatrix} \sum_{\alpha=1}^{M} l_\alpha H v_\alpha \\ l_1 H u_1 v_1 \\ l_2 H u_2 v_2 \\ \vdots \\ l_M H u_M v_M \\ l_1 H v_1^2 + \frac{1}{2} g l_1 H^2 \\ l_2 H v_2^2 + \frac{1}{2} g l_2 H^2 \\ \vdots \\ l_M H v_M^2 + \frac{1}{2} g l_M H^2 \end{pmatrix},$$

$$
\mathbf{Q}(\mathbf{W}) = \begin{pmatrix} 0 \\ -gl_1 H \dfrac{\partial B}{\partial x} + \omega_c l_1 H v_1 \\ -gl_2 H \dfrac{\partial B}{\partial x} + \omega_c l_2 H v_2 \\ \vdots \\ -gl_M H \dfrac{\partial B}{\partial x} + \omega_c l_M H v_M \\ -gl_1 H \dfrac{\partial B}{\partial y} - \omega_c l_1 H u_1 \\ -gl_2 H \dfrac{\partial B}{\partial y} - \omega_c l_2 H u_2 \\ \vdots \\ -gl_M H \dfrac{\partial B}{\partial y} - \omega_c l_M H u_M \end{pmatrix}, \quad \mathbf{R}(\mathbf{W}) = \begin{pmatrix} 0 \\ \mathcal{F}_1^{(u)} + \mathcal{F}_1^{(b)} + \mathcal{F}_1^{(w)} + \mathcal{F}_1^{(\mu)} + \mathcal{F}_1^{(\nu)} \\ \mathcal{F}_2^{(u)} + \mathcal{F}_2^{(b)} + \mathcal{F}_2^{(w)} + \mathcal{F}_2^{(\mu)} + \mathcal{F}_2^{(\nu)} \\ \vdots \\ \mathcal{F}_M^{(u)} + \mathcal{F}_M^{(b)} + \mathcal{F}_M^{(w)} + \mathcal{F}_M^{(\mu)} + \mathcal{F}_M^{(\nu)} \\ \mathcal{G}_1^{(u)} + \mathcal{G}_1^{(b)} + \mathcal{G}_1^{(w)} + \mathcal{G}_1^{(\mu)} + \mathcal{G}_1^{(\nu)} \\ \mathcal{G}_2^{(u)} + \mathcal{G}_2^{(b)} + \mathcal{G}_2^{(w)} + \mathcal{G}_2^{(\mu)} + \mathcal{G}_2^{(\nu)} \\ \vdots \\ \mathcal{G}_M^{(u)} + \mathcal{G}_M^{(b)} + \mathcal{G}_M^{(w)} + \mathcal{G}_M^{(\mu)} + \mathcal{G}_M^{(\nu)} \end{pmatrix}.
$$

Notice that for a well posed problem the system (2.18) has to be solved in a time interval $[0, T]$, in a two-dimensional space domain Ω with boundary Γ, and equipped with given boundary and initial conditions.

3 The Eulerian-Lagrangian method

The time integration of the system (2.18) can be carried out using splitting methods, compare [25, 29] for a first-order splitting method. In the present work we consider a second-order splitting method studied in [32]. Thus, to integrate the equations (2.18) in time we divide the time interval into N sub-intervals $[t_n, t_{n+1}]$ with length $\Delta t = t_{n+1} - t_n$ for $n = 0, 1, \ldots, N$. We also use the notation W^n to denote the value of a generic function W at time t_n. The considered operator splitting method consists of three stages given by:

Stage 1:

$$
\begin{aligned} \frac{\partial \mathbf{W}^*}{\partial t} &= \mathbf{R}(\mathbf{W}^*), \qquad t \in (t_n, t_{n+1/2}], \\ \mathbf{W}^*(t_n) &= \mathbf{W}(t_n). \end{aligned} \tag{3.1}
$$

Stage 2:

$$
\begin{aligned} \frac{\partial \mathbf{W}^{**}}{\partial t} + \frac{\partial \mathbf{F}(\mathbf{W}^{**})}{\partial x} + \frac{\partial \mathbf{G}(\mathbf{W}^{**})}{\partial y} &= \mathbf{Q}(\mathbf{W}^{**}), \qquad t \in (t_n, t_{n+1}], \\ \mathbf{W}^{**}(t_n) &= \mathbf{W}^*(t_{n+1/2}). \end{aligned} \tag{3.2}
$$

Stage 3:

$$
\begin{aligned} \frac{\partial \mathbf{W}^{***}}{\partial t} &= \mathbf{R}(\mathbf{W}^{***}), \qquad t \in (t_{n+1/2}, t_{n+1}], \\ \mathbf{W}^{***}(t_{n+1/2}) &= \mathbf{W}^{**}(t_{n+1}). \end{aligned} \tag{3.3}
$$

The time integration of the system is complete once a time stepping scheme is applied to the above three stages. It is evident that the nonlinear terms and the vertical diffusion are dealt with in the first and third stages whereas, only linear terms are accounted for in the second stage of the splitting. To avoid solution of linear systems of algebraic equations associated with implicit time stepping, we consider only explicit time integration methods for the stages (3.1)-(3.3). Here, we use the explicit third-order Runge-Kutta method studied in [28]. Hence, the procedure to advance the solution of an ordinary differential equation of the structure (3.1) from the time t_n to the next time t_{n+1} can be carried out as

$$\begin{aligned}
\mathcal{W}^{(1)} &= \mathbf{W}^n + \Delta t \mathbf{R}(\mathbf{W}^n),\\
\mathcal{W}^{(2)} &= \frac{3}{4}\mathbf{W}^n + \frac{1}{4}\mathcal{W}^{(1)} + \frac{1}{4}\Delta t \mathbf{R}(\mathcal{W}^{(1)}),\\
\mathbf{W}^{n+1} &= \frac{1}{3}\mathbf{W}^n + \frac{2}{3}\mathcal{W}^{(2)} + \frac{2}{3}\Delta t \mathbf{R}(\mathcal{W}^{(2)}),
\end{aligned} \tag{3.4}$$

where we have dropped the asterisk of the variables for ease of notation. It should be pointed out that the Runge-Kutta method (3.4) has been widely used for time integration of hyperbolic systems of conservation laws mainly because it can be interpreted as a convex combination of first-order Euler steps which exhibits strong stability properties. As a consequence, the Runge-Kutta method (3.4) is TVD, third-order accurate in time, and stable under the usual Courant-Friedrichs-Lewy (CFL) condition involving eigenvalues of the system under study. However, the calculation of the eigenvalues for the system (2.18) is not trivial and in many flow cases these eigenvalues become complex. Under these flow conditions, the system (2.18) is not hyperbolic and yields to the so-called Kelvin-Helmholtz instability at the interface separating the layers for which most of finite volume methods based on Riemann solvers would fail to resolve. In the present work, the proposed Eulerian-Lagrangian method does not require the calculation of the eigenvalues for the multi-layer system and the selection of time steps can be carried out using the eigenvalues associated with the single-layer shallow water counterparts defined as

$$\lambda_\alpha^\pm = u_\alpha \pm \sqrt{gH}, \qquad \mu_\alpha^\pm = v_\alpha \pm \sqrt{gH}, \qquad \alpha = 1, 2\ldots, M. \tag{3.5}$$

Note that the time step can also be adjusted using the maximum wave speed for the multi-layer shallow water system. This selection guarantees the stability of the method but for a fixed simulation time, it may require more steps than using the selection based on the eigenvalues (3.5).

3.1 The Eulerian step

For the spatial discretization of the stage (3.2) we cover the spatial domain Ω with control volumes $\mathcal{C}_{ij} = [x_{i-\frac{1}{2}}, x_{i+\frac{1}{2}}] \times [y_{j-\frac{1}{2}}, y_{j+\frac{1}{2}}]$ shown in Figure 3.1. The control volumes $\mathcal{C}_{ij}$ are centered at (x_i, y_j) with uniform sizes Δx and Δy for simplicity in the presentation only. For the space discretization of the equations (2.18), we use the notations $\mathbf{W}_{i\pm\frac{1}{2},j}(t) = \mathbf{W}(t, x_{i\pm\frac{1}{2}}, y_j)$, $\mathbf{W}_{i,j\pm\frac{1}{2}}(t) = \mathbf{W}(t, x_i, y_{j\pm\frac{1}{2}})$, and

$$\mathbf{W}_{i,j}(t) = \frac{1}{\Delta x}\frac{1}{\Delta y}\int_{x_{i-\frac{1}{2}}}^{x_{i+\frac{1}{2}}}\int_{y_{j-\frac{1}{2}}}^{y_{i+\frac{1}{2}}} \mathbf{W}(t, x, y)dydx,$$

to denote the point-values and the approximate cell-average of the variable $\mathbf{W}$ at the gridpoint $(t, x_{i\pm\frac{1}{2}}, y_j)$, $(t, x_i, y_{j\pm\frac{1}{2}})$, and (t, x_i, y_j), respectively. Integrating the equation (3.2) with respect to space over the control volume $\mathcal{C}_{i,j}$ shown in Figure 3.1, we obtain the following semi-discrete equation

$$\frac{d\mathbf{W}_{i,j}}{dt} + \frac{\mathbf{F}_{i+1/2,j} - \mathbf{F}_{i-1/2,j}}{\Delta x} + \frac{\mathbf{G}_{i,j+1/2} - \mathbf{G}_{i,j-1/2}}{\Delta y} = \mathbf{Q}_{i,j}, \tag{3.6}$$

where $\mathbf{F}_{i\pm1/2,j} = \mathbf{F}(\mathbf{W}_{i\pm1/2,j})$ and $\mathbf{G}_{i,j\pm1/2} = \mathbf{G}(\mathbf{W}_{i,j\pm1/2})$ are the numerical fluxes at the cell interfaces $x = x_{i\pm1/2}$ and $y = y_{i\pm1/2}$, respectively. In (3.6), $\mathbf{Q}_{i,j}$ is a consistent discretization of the source term $\mathbf{Q}$ in (2.18). To resume the spatial discretization of problem (3.6) one needs to reconstruct the fluxes

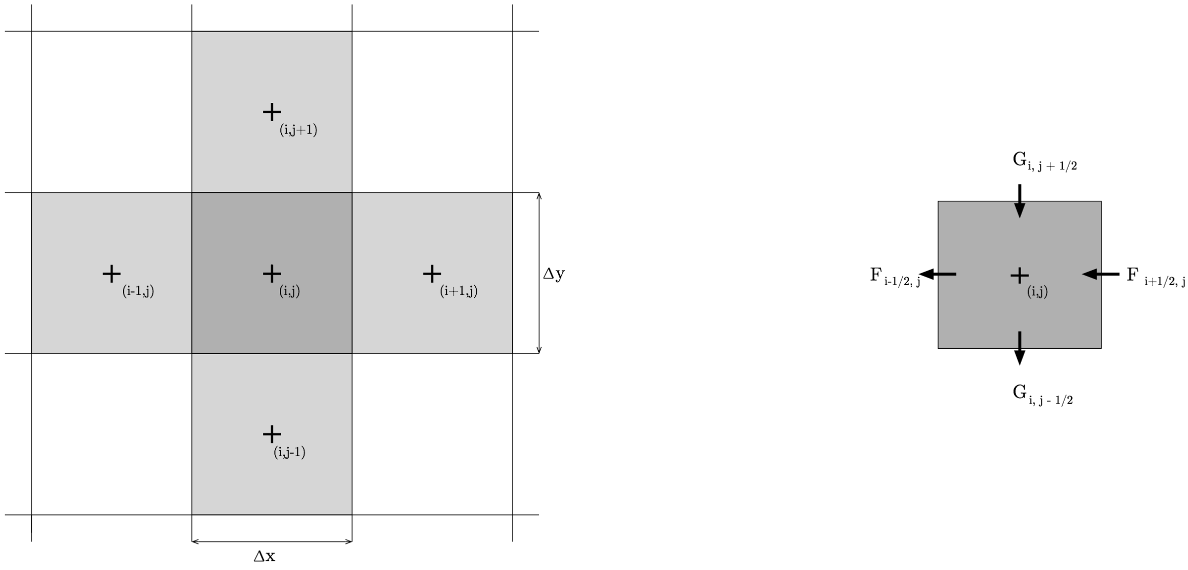

Figure 3.1: The control volume $\mathcal{C}_{i,j}$ used for the spatial discretization.

$\mathbf{F}_{i\pm1/2,j}$ and $\mathbf{G}_{i,j\pm1/2}$. In most finite volume method, this reconstruction involves a solution of Riemann problems at the interfaces $x_{i\pm1/2}$ and $y_{i\pm1/2}$. However, this procedure is computationally demanding and it may restrict the application of the finite volume method to shallow water equations for which Riemann solutions are available. Note that the discretization of equations (3.1) and (3.3) is straightforward and it can be carried out using standard methods.

Integrating (3.2) over the control volume $\mathcal{C}_{ij}$, the basic equations of the finite volume method obtained using the divergence theorem are given by

$$
\begin{aligned}
\frac{\partial}{\partial t}\int_{\mathcal{C}_{i,j}} H \, dV + \sum_{\alpha=1}^{M} \oint_{\mathcal{S}_{i,j}} \left(l_\alpha H u_\alpha n_x + l_\alpha H v_\alpha n_y\right) \, dS = 0,& \\
\frac{\partial}{\partial t}\int_{\mathcal{C}_{i,j}} l_\alpha H u_\alpha \, dV + \oint_{\mathcal{S}_{i,j}} \left(\left(l_\alpha H u_\alpha^2 + \frac{1}{2} g l_\alpha H^2\right) n_x + H u_\alpha v_\alpha n_y\right) dS =& \\
-g l_\alpha H \oint_{\mathcal{S}_{i,j}} B n_x \, dS + \int_{\mathcal{C}_{i,j}} \omega_c l_\alpha H v_\alpha \, dV,& \\
\frac{\partial}{\partial t}\int_{\mathcal{C}_{i,j}} l_\alpha H v_\alpha \, dV + \oint_{\mathcal{S}_{i,j}} \left(H u_\alpha v_\alpha n_x + \left(l_\alpha H v_\alpha^2 + \frac{1}{2} g l_\alpha H^2\right) n_y\right) dS =& \\
-g l_\alpha H \oint_{S_i} B n_y \, dS - \int_{\mathcal{C}_{i,j}} \omega_c l_\alpha H u_\alpha \, dV,&
\end{aligned}
$$

where $\eta = (n_x, n_y)^T$ denotes the unit outward normal to the surface $\mathcal{S}_{i,j}$ of the control volume $\mathcal{C}_{ij}$. Using the local cell outward normal η and tangential $\tau = \eta^\perp$ depicted in Figure 3.2, the above equations can

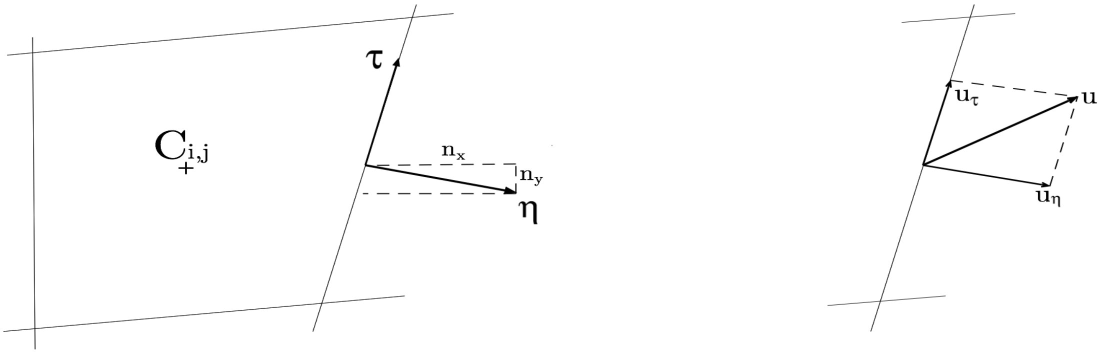

Figure 3.2: The projected velocities on the control volume $\mathcal{C}_{i,j}$.

be projected as

$$\frac{\partial}{\partial t}\int_{\mathcal{C}_{i,j}} H\, dV + \sum_{\alpha=1}^{M}\oint_{\mathcal{S}_{i,j}} l_\alpha H u_{\alpha,\eta}\, dS = 0, \tag{3.7a}$$

$$\frac{\partial}{\partial t}\int_{\mathcal{C}_{i,j}} l_\alpha H u_\alpha\, dV + \oint_{\mathcal{S}_{i,j}}\left(l_\alpha H u_\alpha u_{\alpha,\eta} + \frac{1}{2} g l_\alpha H^2 n_x\right) dS = -g l_\alpha H \oint_{S_i} B n_x\, dS + \int_{\mathcal{C}_{i,j}} \omega_c l_\alpha H v_\alpha\, dV, \tag{3.7b}$$

$$\frac{\partial}{\partial t}\int_{\mathcal{C}_{i,j}} l_\alpha H v_\alpha\, dV + \oint_{\mathcal{S}_{i,j}}\left(l_\alpha H v_\alpha u_{\alpha,\eta} + \frac{1}{2} g l_\alpha H^2 n_y\right) dS = -g l_\alpha H \oint_{S_i} B n_y\, dS - \int_{\mathcal{C}_{i,j}} \omega_c l_\alpha H u_\alpha\, dV, \tag{3.7c}$$

where the normal projected velocity $u_{\alpha,\eta} = u_\alpha n_x + v_\alpha n_y$ and the tangential projected velocity $u_{\alpha,\tau} = v_\alpha n_x - u_\alpha n_y$. In order to simplify the system (3.7), we first sum the equation (3.7b) multiplied by n_x to the equation (3.7c) multiplied by n_y, then we subtract the equation (3.7b) multiplied by n_y from the equation (3.7c) multiplied by n_x. These operations result in

$$\begin{aligned}
\frac{\partial}{\partial t}\int_{\mathcal{C}_{i,j}} H\, dV + \sum_{\alpha=1}^{M}\oint_{\mathcal{S}_{i,j}} l_\alpha H u_{\alpha,\eta}\, dS &= 0,\\
\frac{\partial}{\partial t}\int_{\mathcal{C}_{i,j}} l_\alpha H u_{\alpha,\eta}\, dV + \oint_{\mathcal{S}_{i,j}}\left(l_\alpha H u_{\alpha,\eta} u_{\alpha,\eta} + \frac{1}{2} g l_\alpha H^2\right) dS &= -g l_\alpha H \oint_{S_i} B\, dS + \int_{\mathcal{C}_{i,j}} \omega_c l_\alpha H u_{\alpha,\tau}\, dV,\\
\frac{\partial}{\partial t}\int_{\mathcal{C}_{i,j}} l_\alpha H u_{\alpha,\tau}\, dV + \oint_{\mathcal{S}_{i,j}} l_\alpha H u_{\alpha,\tau} u_{\alpha,\eta}\, dS &= -\int_{\mathcal{C}_{i,j}} \omega_c l_\alpha H u_{\alpha,\eta}\, dV,
\end{aligned}$$

which can be rewritten in a differential form as

$$\begin{aligned}
\frac{\partial H}{\partial t} + \sum_{\alpha=1}^{M}\frac{\partial}{\partial \eta}\left(l_\alpha H u_{\alpha,\eta}\right) &= 0,\\
\frac{\partial}{\partial t}\left(l_\alpha H u_{\alpha,\eta}\right) + \frac{\partial}{\partial \eta}\left(l_\alpha H u_{\alpha,\eta}^2 + \frac{1}{2} g l_\alpha H^2\right) &= -g l_\alpha H \frac{\partial B}{\partial \eta} - \omega_c l_\alpha H u_{\alpha,\tau},\\
\frac{\partial}{\partial t}\left(l_\alpha H u_{\alpha,\tau}\right) + \frac{\partial}{\partial \eta}\left(l_\alpha H u_{\alpha,\eta} u_{\alpha,\tau}\right) &= \omega_c l_\alpha H u_{\alpha,\eta}.
\end{aligned} \tag{3.8}$$

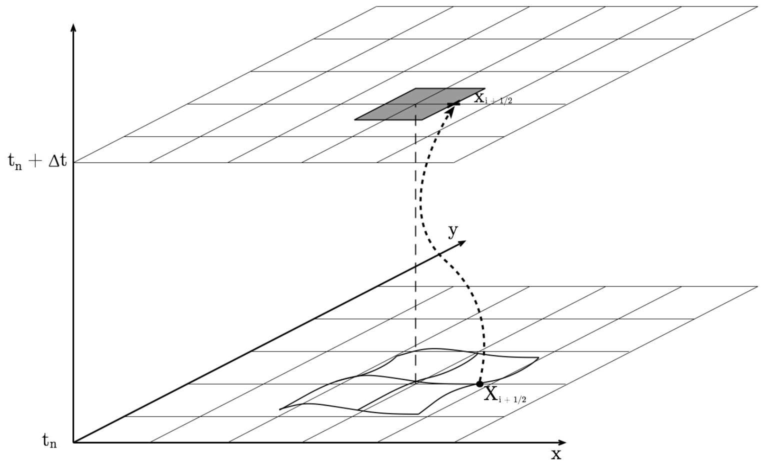

Figure 3.3: Illustration of the method of characteristics: An Eulerian gridpoint $x_{i+1/2}$ is traced back in time to $X_{i+1/2}$ where the intermediate solution $\widehat{U}^n_{i+1/2,j}$ is interpolated.

The system (3.8) can also be reformulated in a non-conservative form as

$$\begin{aligned} \frac{D_0 H}{Dt} + \sum_{\alpha=1}^{M} l_\alpha H \frac{\partial u_{\alpha,\eta}}{\partial \eta} &= 0, \\ \frac{D_\alpha u_{\alpha,\eta}}{Dt} + g\frac{\partial H}{\partial \eta} &= -g\frac{\partial B}{\partial \eta} - \omega_c u_{\alpha,\tau}, \\ \frac{D_\alpha u_{\alpha,\tau}}{Dt} + H\frac{\partial u_{\alpha,\tau}}{\partial \eta} &= \omega_c u_{\alpha,\eta}, \end{aligned} \tag{3.9}$$

where $\frac{D_\zeta}{Dt}$ is the total material derivative defined as

$$\frac{D_\zeta}{Dt} = \frac{\partial}{\partial t} + U_\zeta \frac{\partial}{\partial \eta}, \qquad \zeta = 0, 1, \dots, M, \tag{3.10}$$

with

$$U_\zeta = \begin{cases} \displaystyle\sum_{\alpha=1}^{M} l_\alpha u_{\alpha,\eta}, & \text{if} \quad \zeta = 0, \\ u_{\zeta,\eta}, & \text{if} \quad \zeta = 1, 2, \dots, M. \end{cases} \tag{3.11}$$

Notice that the above projection techniques simplify the solution of two-dimensional shallow water equations (3.2) in the control volume $\mathcal{C}_{i,j}$ to the solution of one-dimensional system (3.9) on each surface $\mathcal{S}_{i,j}$ of this control volume. A similar projection procedure on general meshes has been proposed in [7] among others. It should be stressed that the projected system (3.9) is used in our approach only to reconstruct the numerical fluxes in the finite volume method solution of the conservative system (3.2).

3.2 The Lagrangian step

To approximate the numerical fluxes $\mathbf{F}_{i\pm1/2,j}$ and $\mathbf{G}_{i,j\pm1/2}$ in (3.6) we consider the modified method of characteristics applied to the projected system (3.9). In general, this method consists of imposing a regular grid at the new time level and backtracking the flow trajectories to the previous time level, see for instance [24, 8]. The solutions at the old time level are obtained using interpolation from their known values on a regular grid. Hence, for each layer ζ and gridpoint $x_{i+1/2}$ we calculate the characteristic curves $X_{\zeta,i+1/2}(s)$ associated with the equations (3.9) by solving the initial-value problems

$$\begin{aligned} \frac{dX_{\zeta,i+1/2}(s)}{ds} &= U_{\zeta,}\Big(s, X_{\zeta,i+1/2}(s), y_j\Big), \qquad s \in [t_n, t_{n+1}], \\ X_{\zeta,i+1/2}(t_{n+1}) &= x_{i+1/2}, \end{aligned} \tag{3.12}$$

with similar initial-value problems for the characteristic curves $Y_{\zeta,j+1/2}(s)$ related to the gridpoint $y_{j+1/2}$

$$\begin{aligned} \frac{dY_{\zeta,j+1/2}(s)}{ds} &= U_{\zeta,}\Big(s, x_i, Y_{\zeta,j+1/2}(s)\Big), \qquad s \in [t_n, t_{n+1}], \\ Y_{\zeta,j+1/2}(t_{n+1}) &= y_{j+1/2}, \end{aligned} \tag{3.13}$$

As shown in Figure 3.3, $X_{\zeta,i+1/2}(s)$ and $Y_{\zeta,j+1/2}(s)$ are the departure points at time s of a particle that will arrive in the time t_{n+1} at the gridpoint $x_{i+1/2}$ and $y_{j+1/2}$ respectively. In our simulations we used the third-order Runge-Kutta method (3.4) for the solution of the initial-value problems (3.12) and (3.13). In general $X_{\zeta,i+1/2}(t_n)$ and $Y_{\zeta,j+1/2}(t_n)$ will not coincide with the spatial position of a gridpoint. Hence, once the characteristic curves $X_{\zeta,i+1/2}(t_n)$ and $Y_{\zeta,j+1/2}(t_n)$ are accurately calculated, the intermediate solutions $W^n_{i+1/2,j}$ and $W^n_{i,j+1/2}$ of a function W are reconstructed using

$$W^n_{i+1/2,j} = \widehat{W}^n_{i+1/2,j}, \qquad W^n_{i,j+1/2} = \widehat{W}^n_{i,j+1/2}, \tag{3.14}$$

where $\widehat{W}^n_{i+1/2,j} = W\left(t_n, X_{\zeta,i+1/2}(t_n), y_j\right)$ and $\widehat{W}^n_{i,j+1/2} = W\left(t_n, x_i, Y_{\zeta,j+1/2}(t_n)\right)$ are the solutions at the departure points obtained by interpolation from the gridpoints of the control volume where these departure points belong, see Figure 3.3. For example, a Lagrange-based interpolation polynomial can be formulated as

$$\widehat{W}^n_{i+1/2,j} = \sum_{k,l} \mathcal{L}_{k,l}\left(X_{\zeta,i+1/2}, y_j\right) W^n_{k,l}, \qquad \widehat{W}^n_{i,j+1/2} = \sum_{k,l} \mathcal{L}_{k,l}\left(x_i, Y_{\zeta,j+1/2}\right) W^n_{k,l}, \tag{3.15}$$

with $\mathcal{L}_{k,l}$ are the Lagrange polynomials defined as

$$\mathcal{L}_{k,l}(x,y) = \prod_{\substack{p=0\\p\neq k}} \prod_{\substack{q=0\\q\neq l}} \frac{x - x_p}{x_k - x_p} \frac{y - y_q}{y_l - y_q}.$$

Notice that other high-order interpolation methods can also be used in (3.15). In the present work, the Lagrange interpolation (3.15) guarantees a second-order accuracy for the proposed Eulerian-Lagrangian finite volume method. Assume that the departure points $X_{\zeta,i+1/2}(t_n)$ and $Y_{\zeta,j+1/2}(t_n)$ are accurately approximated, the first stage (predictor step) of the solution of the multilayer shallow water system (3.9) in the Eulerian Lagrangian method is defined as

$$\begin{aligned} H^n_{i+1/2,j} &= \widehat{H}^n_{i+1/2,j} - \frac{\Delta t}{\Delta x}\widehat{h}^n_{i+1/2,j}\left((u_{\alpha,\eta})^n_{i+1,j} - (u_{\alpha,\eta})^n_{i,j}\right), \\ (u_{\alpha,\eta})^n_{i+1/2,j} &= (\widehat{u}_{\alpha,\eta})^n_{i+1/2,j} - g\frac{\Delta t}{\Delta x}\Big((h^n + Z)_{i+1,j} - (h^n + Z)_{i,j}\Big) - \Delta t\omega_c\left(\widehat{u}_{\alpha,\tau}\right)^n_{i+1/2,j}, \\ (u_{\alpha,\tau})^n_{i+1/2,j} &= (\widehat{u}_{\alpha,\tau})^n_{i+1/2,j} - \frac{\Delta t}{\Delta x}\widehat{h}^n_{i+1/2,j}\left((u_{\alpha,\tau})^n_{i+1,j} - (u_{\alpha,\tau})^n_{i,j}\right) + \Delta t\omega_c\left(\widehat{u}_{\alpha,\eta}\right)^n_{i+1/2,j}, \end{aligned} \tag{3.16}$$

where

$$\widehat{H}^n_{i+1/2,j} = H\left(t_n, X_{\alpha,i+1/2}(t_n), y_j\right), \qquad (\widehat{u}_{\alpha,\eta})^n_{i+1/2,j} = u_{\alpha,\eta}\left(t_n, X_{\alpha,i+1/2}(t_n), y_j\right),$$

$$(\widehat{u}_{\alpha,\tau})^n_{i+1/2,j} = u_{\alpha,\tau}\left(t_n, X_{\alpha,i+1/2}(t_n), y_j\right).$$

The intermediate states in the y-direction $H^n_{i,j+1/2}$, $(u_{\alpha,\eta})^n_{i,j+1/2}$ and $(u_{\alpha,\tau})^n_{i,j+1/2}$ are calculated in the same way. When the projected states are calculations are complete, the states $\mathbf{W}^n_{i\pm1/2,j}$ and $\mathbf{W}^n_{i,j\pm1/2}$ are determined by using $v_\alpha = (u_{\alpha,\tau}, u_{\alpha,\eta}) \cdot \eta$ and $u_\alpha = (u_{\alpha,\tau}, u_{\alpha,\eta}) \cdot \tau$.

Using the concept of C-property the discretization of the source terms $\mathbf{Q}_{i,j}$ is carried so that the discretized source terms are well balanced with the discretized flux gradients, for further explanation see [9, 8]. Recall that a numerical scheme is said to satisfy the C-property for the equations (3.2) if the condition

$$H^n + B = C = constant, \qquad u^n_\alpha = v^n_\alpha = 0, \qquad \alpha = 1, 2, \ldots, M, \tag{3.17}$$

this is correct for flows at rest. The source terms are thus reconstructed such that the condition (3.17) is preserved after discretization. Using the same method as reported in [9, 4], for one-dimensional shallow water equations, the terms are discretized as follows

$$\begin{aligned} \left(gH\frac{\partial B}{\partial x}\right)^n_{i,j} &= g\frac{H^n_{i+1/2,j} + H^n_{i-1/2,j}}{2}\frac{B^n_{i+1,j} - B^n_{i-1,j}}{2\Delta x}, \\ \left(gh\frac{\partial B}{\partial y}\right)^n_{i,j} &= g\frac{H^n_{i,j+1/2} + H^n_{i,j-1/2}}{2}\frac{B^n_{i,j+1} - B^n_{i,j-1}}{2\Delta y}, \end{aligned} \tag{3.18}$$

where the averaged solutions are defined by

$$H^n_{i+1/2,j} = \frac{H^n_{i+1,j} + H^n_{i-1,j}}{2}, \qquad H^n_{i,j+1/2} = \frac{H^n_{i,j+1} + Hh^n_{i,j-1}}{2}.$$

By projecting the original shallow water model into the local system and using dimension-by-dimension discretization, the source terms (3.18) can be discretized in the same manner as [9]. For further detail on this method please see [9].

4 Numerical Results

The numerical results for four two-dimensional multilayer shallow water flow test cases are presented in this section. The aim is to demonstrate the accuracy and adaptability of the scheme detailed above. In the first test case we examine the conservation property of the scheme, using a free-surface flow at rest on a bed of non-flat topography. In the second, a simple dam-break problem is posed and the results are compared to those of a three-dimensional Navier-Stokes equations. We also examine a circular dam-break over flat and non-flat topography. Finally we simulate wind driven flow in two dimensions. In all our computations the total water height H is given by the initial conditions, and the water heights h_α of each layer is defined (using equal factions) as

$$h_\alpha = l_\alpha H \qquad \text{with} \qquad l_\alpha = \frac{1}{M}, \qquad \alpha = 1, \ldots, M.$$

In addition, a fixed courant number CFL $= 0.8$ is used whereas the time step Δt varies according to the stability condition

$$\Delta t = \text{CFL}\frac{\min(\Delta x, \Delta y)}{\max\limits_{\alpha}\left(|u^n_\alpha| + \sqrt{gH}, |v^n_\alpha| + \sqrt{gH}\right)}.$$

The implementation of boundary conditions is performed using techniques similar to those described in [7]. For the computational examples considered in this section, boundary conditions are enforced on the corrector solution by computing fluxes at cell boundaries. On the predictor solution, boundary conditions are enforced in boundary cells by setting the required variables to the corresponding values of the adjacent inner cells.

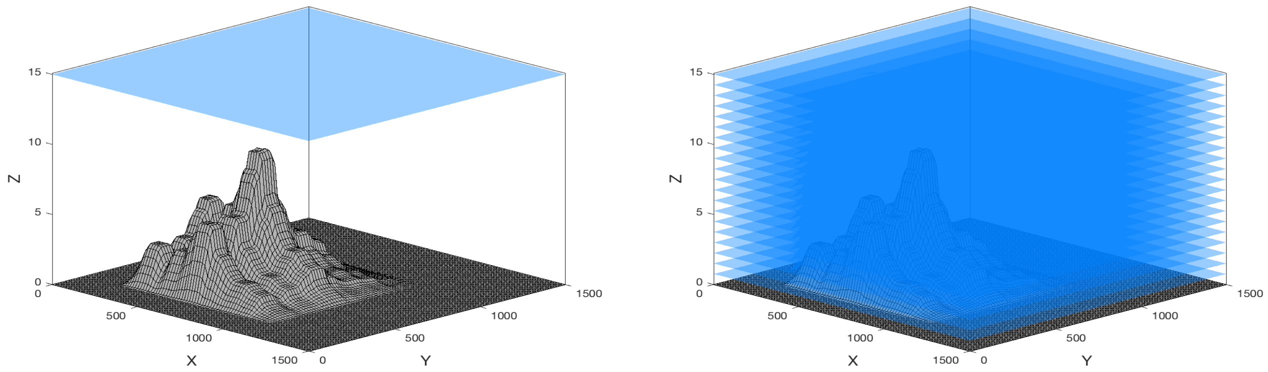

Figure 4.1: Water free-surface and interfaces for the multilayer flow problem at rest at time $t = 10800$ s using single-layer and 10-layer models.

In all results presented in this section the linear interpolation procedure is used in the predictor stage. Along with the water heights h_α, water free-surface H and the water velocities (u_α, v_α) we also present results for the vertical velocity w. The three-dimensional velocity fields are calculated using two-dimensional results, by implementing a similar post-processing method as in [6, 4]. Hence, the vertical velocity w is computed from the divergence-free condition

$$\frac{\partial u}{\partial x} + \frac{\partial v}{\partial y} + \frac{\partial w}{\partial z} = 0. \tag{4.1}$$

Integrating the equation (4.1) in a control volume yields

$$w^n_{\alpha+1,i,j} = w^n_{\alpha,i,j} + \Delta z \left(\frac{u^n_{\alpha,i+1/2,j} - u^n_{\alpha,i-1/2,j}}{\Delta x} + \frac{u^n_{\alpha,i+1/2,j+1/2} - u^n_{\alpha,i+1/2,j+1/2}}{\Delta y} \right)$$

where $\Delta z = \frac{h_{\alpha+1}+h_\alpha}{2}$ is the spatial in the vertical direction between two layers. On the bottom boundary we use non-penetration boundary conditions. A similar procedure has also been used in [15] for one-dimensional multilayer shallow water equations.

4.1 Lake at multilayer rest flow

Lake at rest flow has been introduced in [10] to check the well-balance property of a finite volume method for single-layer one-dimensional shallow water equations. In this example we reconstruct a similar test problem but for two-dimensional shallow water flows. The idea lies on using Kronecker tensor product of the one-dimensional bed proposed in [10] in x- and y-direction. Hence, we solve the shallow water equations (2.1) with source term associated with the bed only *i.e.*, $\omega_c = 0$ and $F_\alpha = G_\alpha = 0$ and the bed is defined as

$$B(x, y) = \frac{2}{7}\mathcal{B}(x) \otimes \mathcal{B}(y),$$

where $\mathcal{B}$ is the one-dimensional bed defined in [10]. The problem is solved in a squared domain with length of 1500 m and the results are presented at time $t = 10800$ s as in [10]. In practice, the total water free-surface must remain constant and the water velocity should be zero at all times. However, many numerical methods fail to preserve these conditions at the discrete level. In Figure 4.1 we present the results obtained for water free-surface and interfaces using a mesh with 100×100 gridpoints and a 20-layer model. We also include results obtained using the conventional single-layer shallow water equations. As expected, the water free-surface remains constant along the simulation times for all considered models

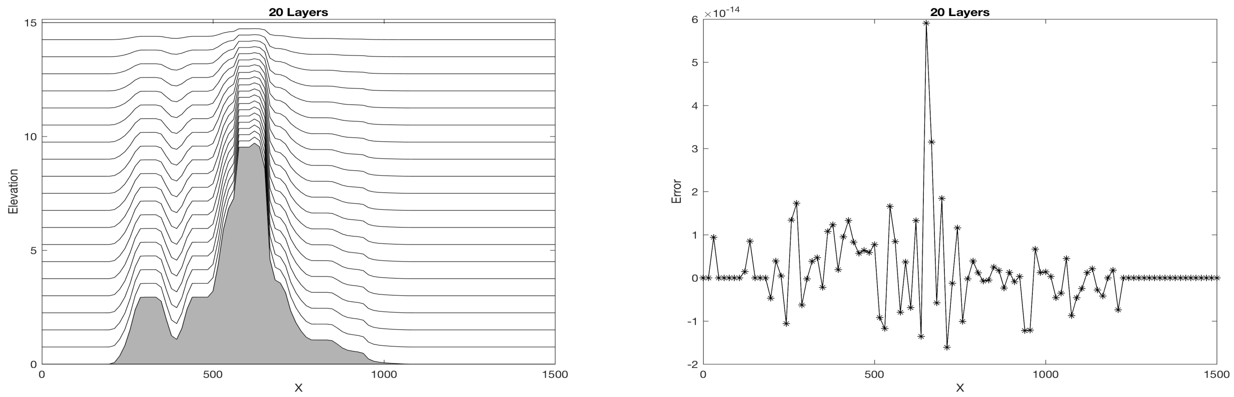

Figure 4.2: Cross-section of the water free-surface and interfaces for the 20-layer flow problem at rest at time $t = 10800$ s (left) and the associated error in the water free-surface (right).

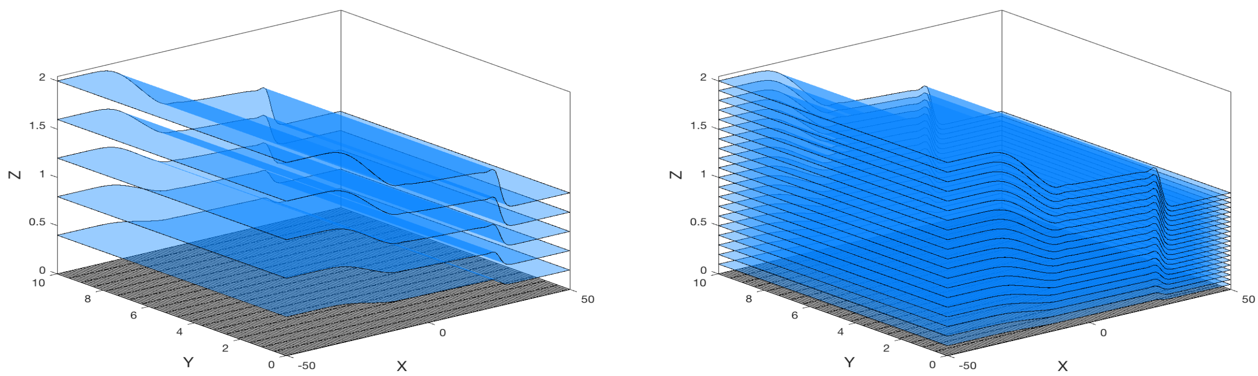

Figure 4.3: Water free-surface and interfaces for the multilayer dam-break problem on a flat bottom at time $t = 14$ s using 5-layer model (left) and 20-layer model (right).

and no disturbances have been detected over the irregular two-dimensional bed. In addition, increasing the number of layers in the model has not deteriorated the response of the water free-surface in the lake.

In Figure 4.2 we present the cross-section along the main diagonal ($y = x$) of the results obtained for the 20-layer model and also the error in the water free-surface as a difference between the numerical and analytical free-surface solutions. It is clear from the results presented in Figure 4.2 that our Eulerian-Lagrangian method preserves constant water free-surface and the errors are practically zero to the machine precision. Similar results not reported here were obtained for 5-layer and 10-layer models. This confirms that the proposed method is well balanced and able to accurately resolve two-dimensional multilayer shallow water flows over an non-flat bottom without relying on complex techniques to balance the discretizations of source terms and flux gradients.

4.2 Multilayer dam-break problem on a flat bottom

Dam-break problems have been mainly modeled using single-layer shallow water equations but recently in [3, 4] one-dimensional multi-layer shallow water equations have been used to simulate a dam-break problem over a flat bottom. In this example we consider the two-dimensional version of this problem in

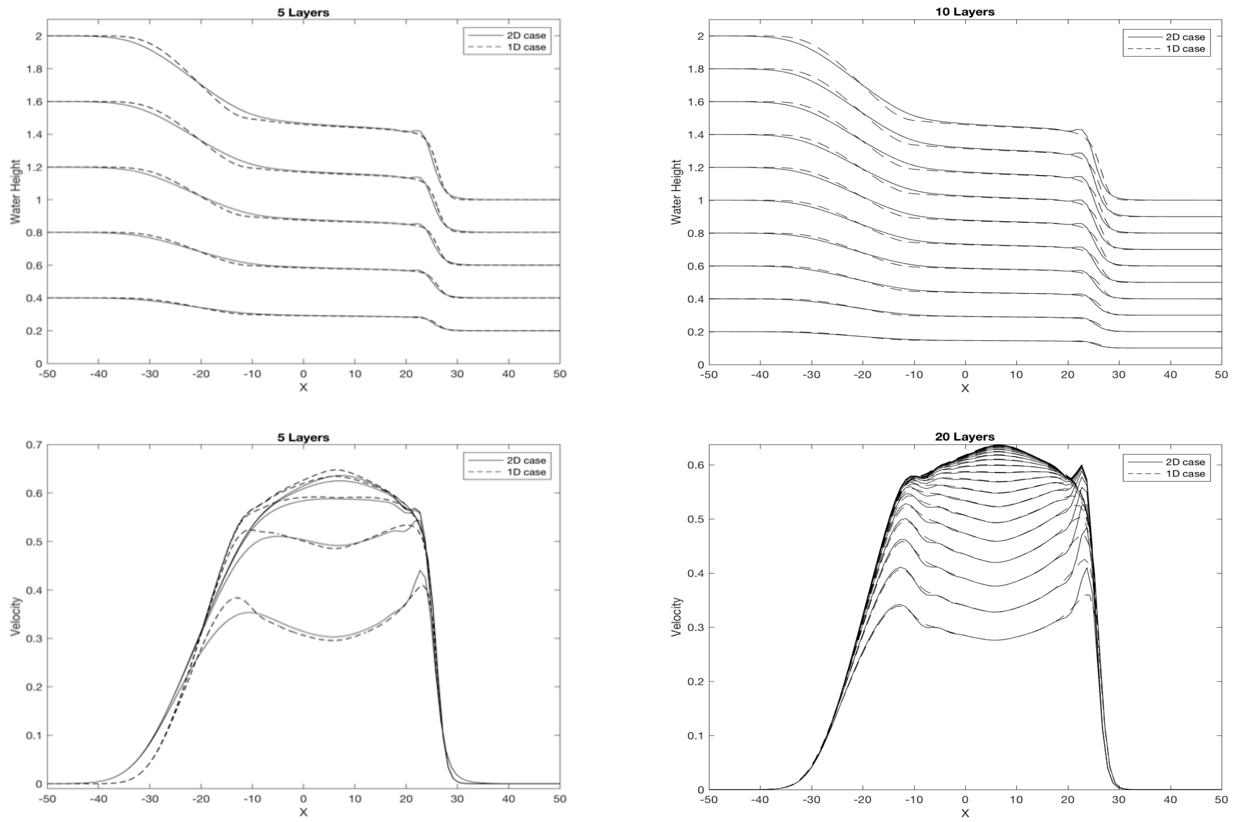

Figure 4.4: Horizontal cross-sections of the water free-surface (top) and water velocity (bottom) for the multilayer dam-break problem on a flat bottom at time $t = 14$ s using different layers in the model.

order to compare our results to those obtained using its one-dimensional counterpart. Thus, we solve the multilayer shallow water equations (2.1) in a flat rectangular channel of length 100 and width 10 subject to the following initial conditions

$$H(0,x,y) = \begin{cases} 2, & \text{if} \quad x \leq 0, \\ 1, & \text{if} \quad x > 0, \end{cases} \qquad\qquad u(0,x,y) = v(0,x,y) = 0.$$

Wind effects and Coriolis forces are neglected in this test example and we use the same parameters as those used in [6, 4] for the one-dimensional case, the viscosity coefficient $\nu = 0.01$, the gravity $g = 2$, the friction coefficient $\kappa = 0.1$ and the results are presented at time $t = 14$ s. The results obtained for this problem, using our Eulerian-Lagrangian method, are also compared to those calculated using the three-dimensional Navier-Stokes equations with free-surface conditions as published in [16].

Figure 4.3 presents the water free-surface and interfaces for the 5-layer and 20-layer models at time $t = 14$ using a mesh with 100×20 gridpoints. As in all dam-break problems, at $t = 0$ the dam breaks and the flow problem consists of a shock wave propagating downstream and a rarefaction wave propagating upstream. The proposed Eulerian-Lagrangian method captures these flow patterns without generating spurious oscillations in the shock area. Under the considered dam-break conditions, it seems that the number of layers in the model has little effects on the flow features, compare the water free-surface profiles obtained for 5-layer and 20-layer models in Figure 4.3. To further emphasis these effects we display in Figure 4.4 horizontal cross-sections of the water free-surface and water velocity at $y = 5$ for the 5-layer and 20-layer models. For comparison reasons we also include in Figure 4.4 the results obtained using the

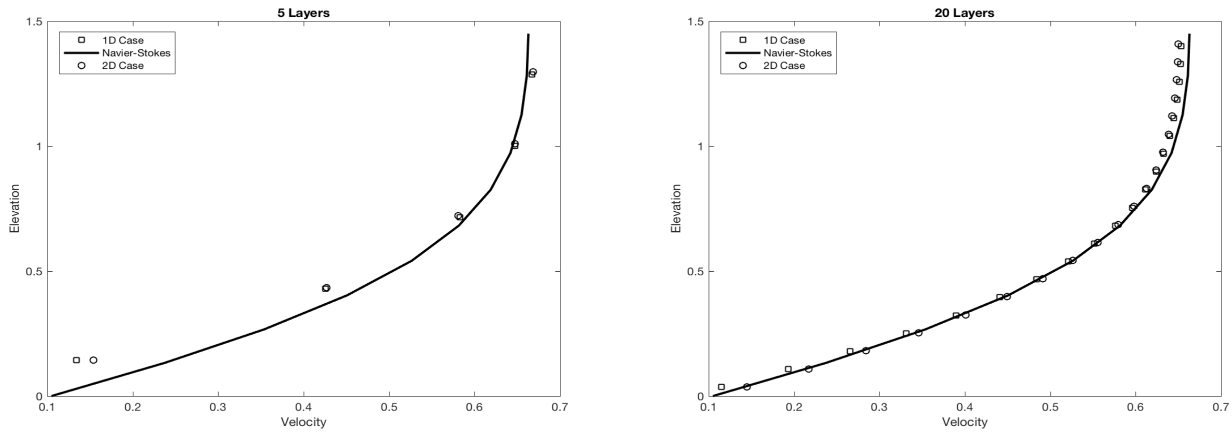

Figure 4.5: Water velocities at the location $(x = 8, y = 5)$ for the multilayer dam-break problem on a flat bottom at time $t = 14$ s using different layers in the model.

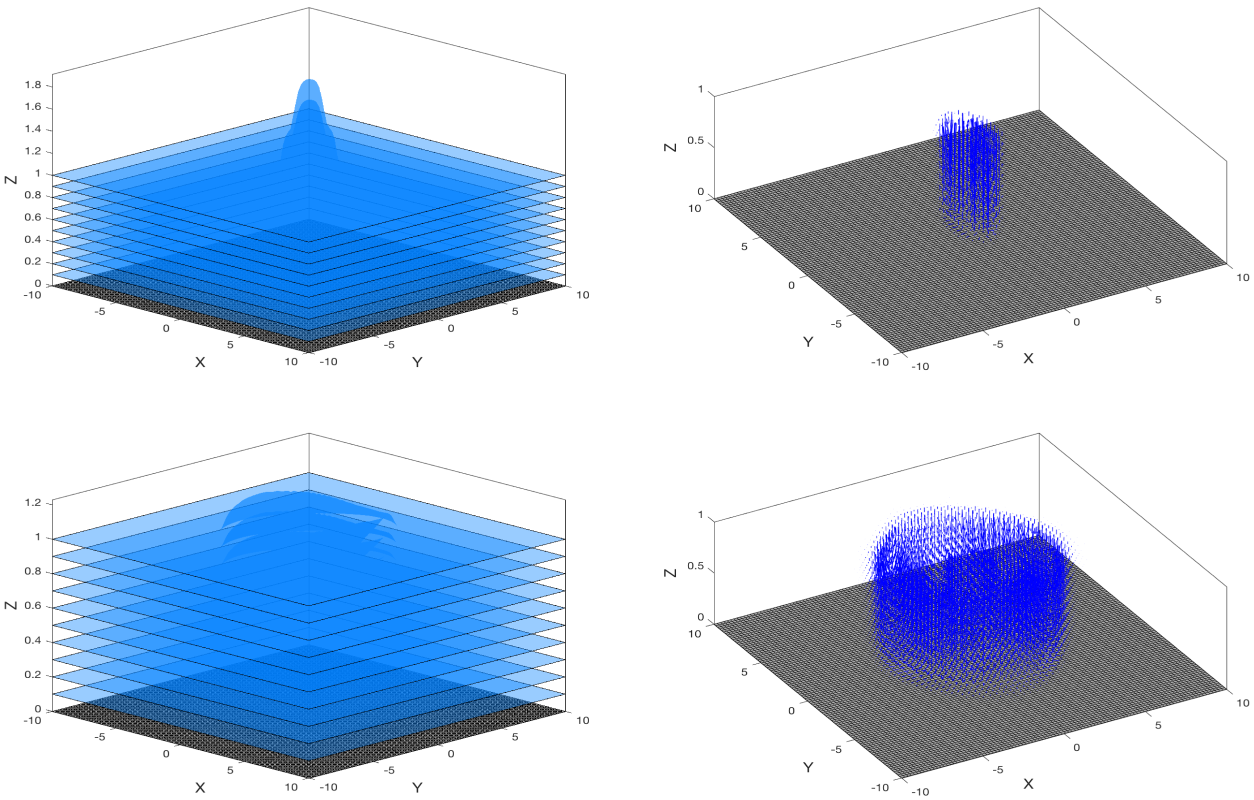

Figure 4.6: Water heights (left) and velocity fields (right) obtained for the multilayer circular dam-break on a flat bottom using 10 layers. From top to bottom $t = 0.1$ and 1.

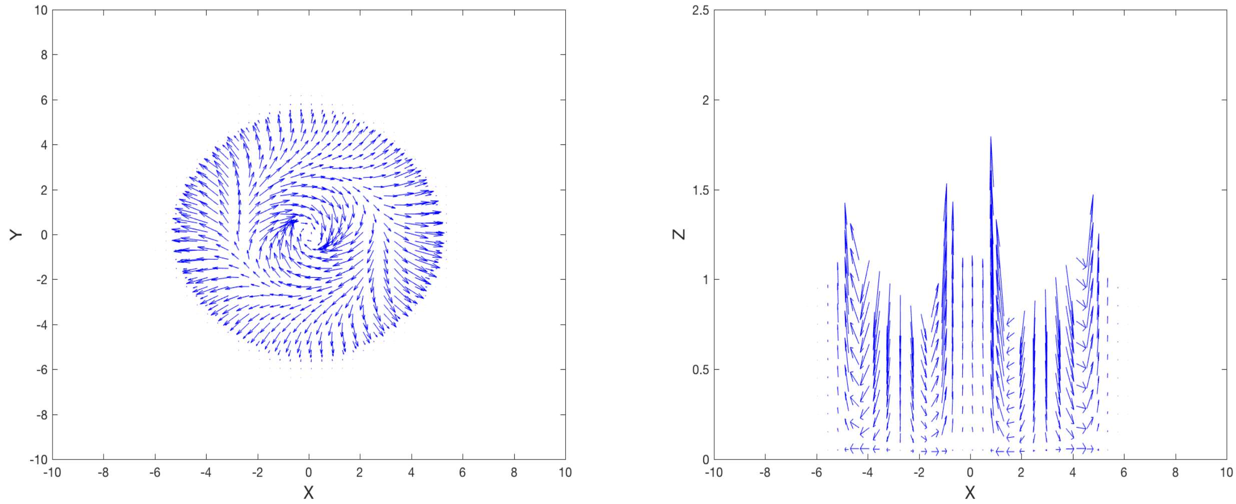

Figure 4.7: Lateral cross-section of the velocity field in the xy-plane at $h = 1$ (left) and vertical cross-section of the velocity field in the xz-plane at $y = 0$ for the multilayer circular dam-break on a flat bottom using 10 layers at $t = 1$.

one-dimensional multi-layer model. As can be seen from these results there is a difference between two-dimensional results and their one-dimensional counterparts. It seems that the two-dimensional results are more diffusive than the one-dimensional results at the rarefaction zone but that at the shock zone the two-dimensional results look sharper than their one-dimensional counterparts. We observe some fluctuations at the hydraulic jump in the results presented in Figure 4.4 which has also been detected in the three-dimensional results obtained using the full Navier-Stokes simulations in [4].

Following the same ideas reported in [4] we compare in Figure 4.5 the results obtained using our two-dimensional multilayer shallow water model to those obtained using the three-dimensional Navier-Stokes equations. In this figure we present the velocity profiles in the location $(x = 8, y = 5)$ at time $t = 14$ for the 5-layer and 20-layer on a mesh with 100×20 gridpoints. For comparison reason, we also include the results obtained using the one-dimensional multilayer shallow water model in this figure. It is clear from the results presented in Figure 4.5 that an increase in the number of layers in both one- and two-dimensional models results in an increase in the accuracy of the obtained results as compared to the full three-dimensional results. Under the considered flow conditions, the two-dimensional results are slightly more accurate than the one-dimensional results. Note that, in terms of the computational cost, solving the two-dimensional multilayer shallow water equations is more efficient than solving the three-dimensional Navier-Stokes equations for dam-break flow problems.

4.3 Multilayer circular dam-break problem

We consider a multilayer circular dam-break problem in a squared domain $[-10, 10] \times [-10, 10]$. The domain is assumed to be flat, the viscosity of water is set to $\nu = 0.05\ m^2/s$, the water density $\rho = 1025\ kg/m^3$, the gravity $g = 9.81\ m/s^2$, the Coriolis coefficient $\omega_c = 1$, and the bed friction coefficient is set to $\kappa = 0.001\ m/s$. Initially,

$$h(0, x, y) = 1 + \frac{1}{2}\left(1 - \tanh\left(\frac{\sqrt{ax^2 + by^2} - 1}{c}\right)\right), \quad u(0, x, y) = v(0, x, y) = 0,$$

where $a = \frac{5}{2}$, $b = \frac{5}{2}$ and $c = 0.1$. A similar problem has been considered in [22] for the standard single-layer circular dam-break problem. Here, the computational domain is discretized into 100×100

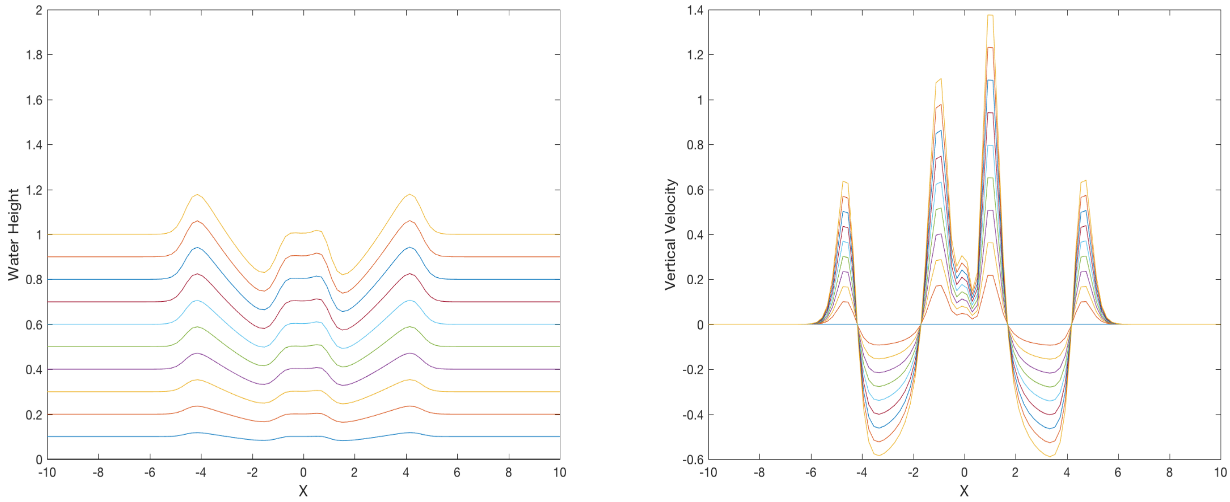

Figure 4.8: Vertical cross-sections at $y = 0$ of water heights (left) and velocity plots (right) for the multilayer circular dam-break on a flat bottom using 10 layers at $t = 1$

gridpoints and obtained results for water heights and velocity fields are presented for different instants. In Figure 4.6 we display the water heights and the velocity fields obtained using 10 layers at time $t = 0.1$ and 1. It is clear from the presented results that the water flows away from deep central region as the rarefaction wave progresses outwards. The Coriolis effect adds an extra rotational effects to the results, though they remain symmetric, as well as retaining a strongly distinguishable wavefront which is to be expected. To emphasis the Coriolis effects on this dam-break problem, we present in Figure 4.7 the lateral and vertical cross-sections of the velocity fields at $h = 1$ and $y = 0$, respectively. The results are presented at the final simulation time $t = 1$. The proposed method is able to accurately resolve the Coriolis effects and to capture the vertical velocities which are vital to the understanding of complex flows presented by this class of dam-break problems. Figure 4.8 further demonstrates the effects of Coriolis term on this multilayer circular dam-break problem. Here, we display the vertical cross-sections at $y = 0$ of water heights and velocity profiles at time $t = 1$. As can be seen, the symmetry is well preserved in the obtained water heights and mixing vertical velocities are also detected in the presented velocity profiles. Note that the velocity profiles in Figure 4.8 are not symmetric because of the Coriolis terms included in the multilayer model. Again the obtained results demonstrate the ability of the considered multilayer models to capture the vertical flow features without relying on the three-dimensional free-surface flow equations.

Next we turn our attention to multilayer circular dam-break problems on non-flat beds. To this end we solve the previous problem over a non-flat bottom defined by

$$B(x, y) = \frac{1}{2}\mathcal{B}_x(x) \otimes \mathcal{B}_y(y),$$

where

$$\mathcal{B}_x(x) = \begin{cases} \sin\left(\frac{\pi}{4}x\right), & \text{if} \quad -4 \le x < 4, \\ 0, & \text{elsewhere}, \end{cases} \qquad \mathcal{B}_y(y) = \begin{cases} -\cos\left(\frac{\pi}{4}y\right), & \text{if} \quad -2 \le y < 2, \\ 0, & \text{elsewhere}. \end{cases}$$

The initial conditions and the flow parameters are the same as in the previous simulations. The main issues we wish to address in this test problem are concerned with the capabilities of the proposed Eulerian-Lagrangian method to solve multilayer circular dam-break problems on non-flat beds. Figure 4.9 exhibits

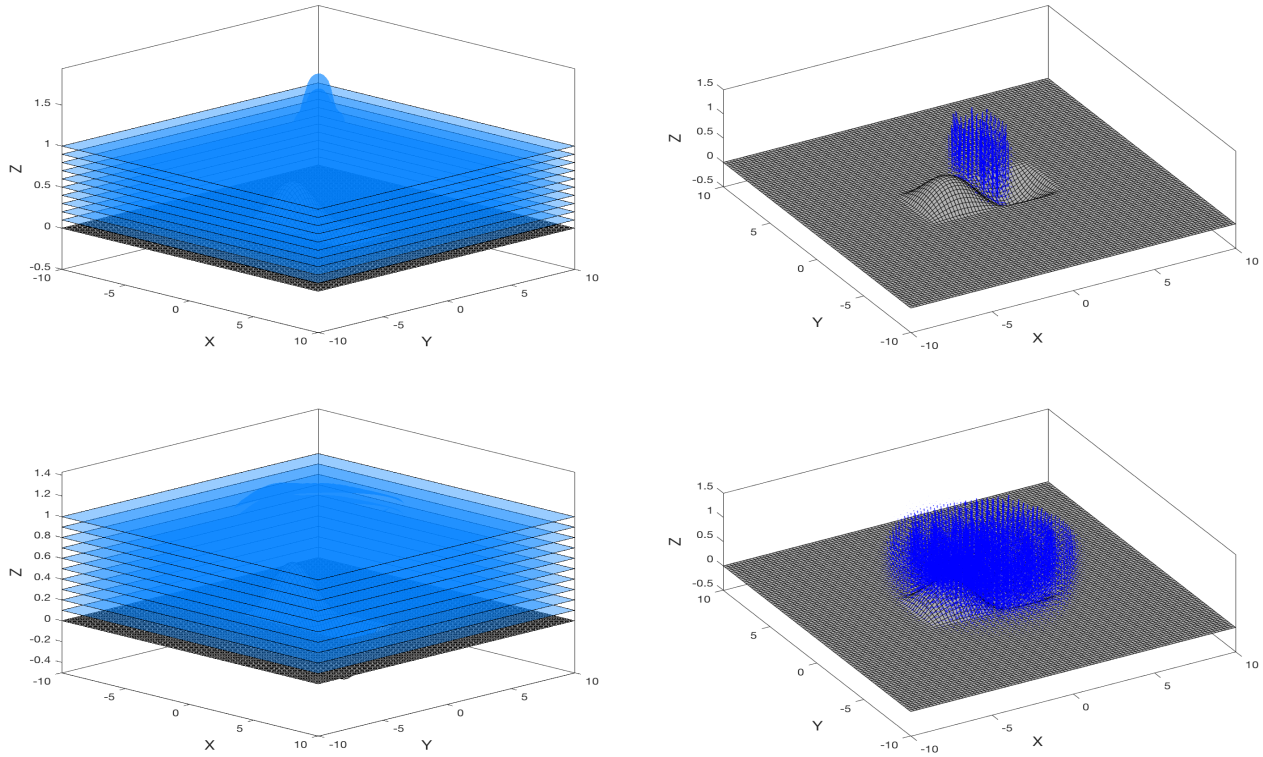

Figure 4.9: Water heights (left) and velocity fields (right) obtained for the multilayer circular dam-break on a non-flat bottom using 10 layers. From top to bottom $t = 0.1$ and 1.

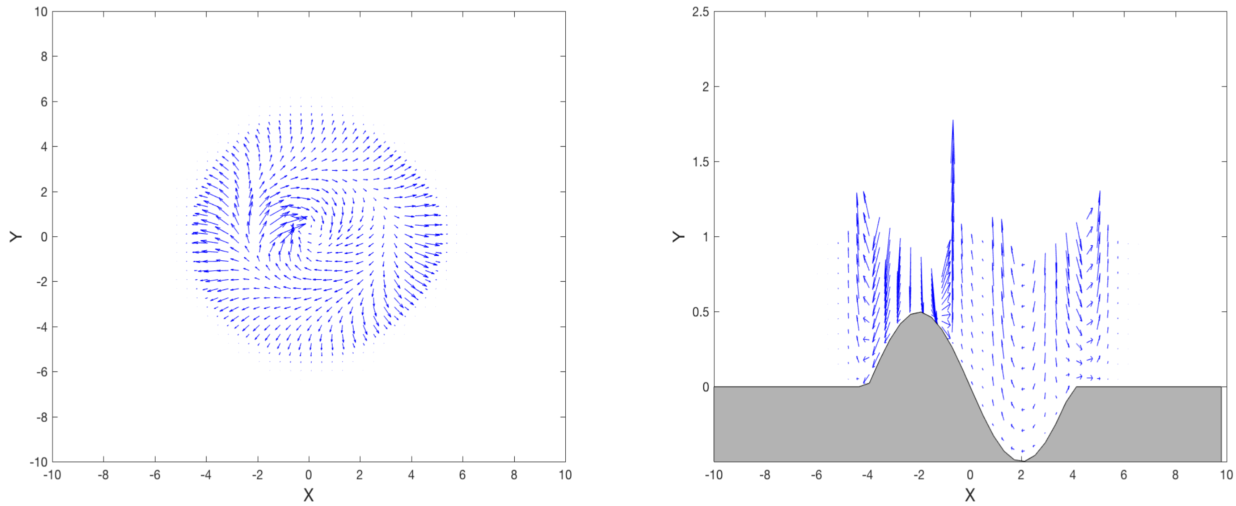

Figure 4.10: Lateral cross-section of the velocity field in the xy-plane at $h = 1$ (left) and vertical cross-section of the velocity field in the xz-plane at $y = 0$ for the multilayer circular dam-break on a non-flat bottom using 10 layers at $t = 1$.

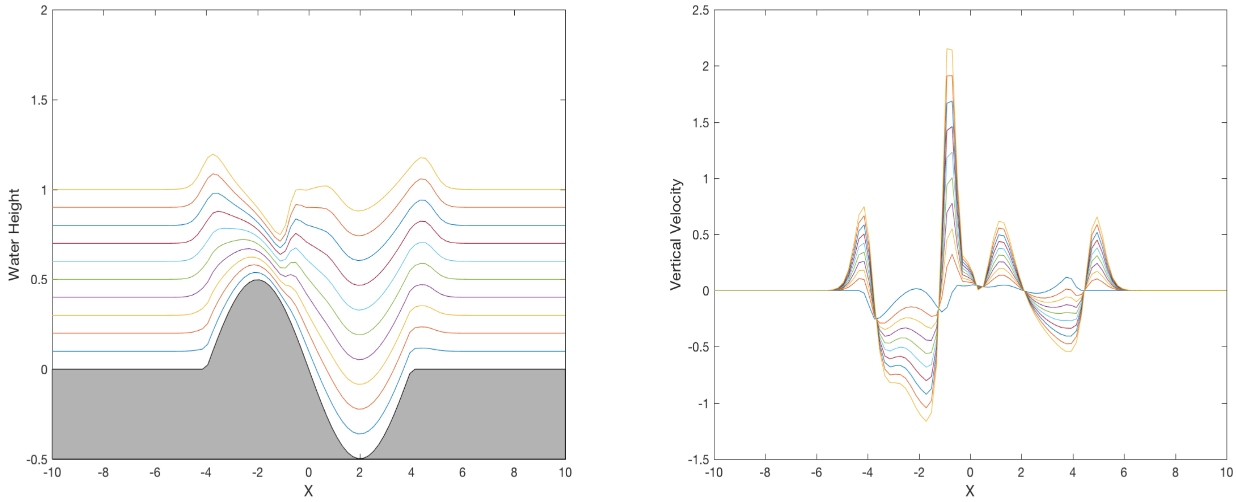

Figure 4.11: Vertical cross-sections at $y = 0$ of water heights (left) and velocity plots (right) for the multilayer circular dam-break on a non-flat bottom using 10 layers at $t = 1$.

the water heights and the velocity fields obtained using 10 layers at time $t = 0.1$ and 1. In Figure 4.10 we display the lateral and vertical cross-sections of the velocity fields at $h = 1$ and $y = 0$, respectively. The vertical cross-sections at $y = 0$ of water heights and velocity profiles at time $t = 1$ are presented in Figure 4.11. Under the actual flow conditions, it is clear from the presented results that the non-flat bathymetry has direct effects on the flow structure. As the dam breaks over the bump the rarefaction wave progresses and both Coriolis and bathymetric terms change its behavior. For example when results in Figure 4.11 are compared to those in Figure 4.8 obtained for flat bottom, it is easy to see the effect the bathymetry has on the vertical velocity and the high water level of variation caused. In addition, Figure 4.10 shows the asymmetry in the flow caused by the varying topography, though it is interesting to note that the rarefaction still progresses at same speed over the non-flat bottom. It is worth noting that the multilayer shallow water equations handle this complex flow problem well for both the flat and non-flat beds and delivering new insights into vertical velocity for a shallow water flows. The proposed Eulerian-Lagrangian method performs very satisfactorily for this flow problem since it does not diffuse the moving fronts and no spurious oscillations have been detected near steep gradients of the water heights in the computational domain.

4.4 Wind-driven circulation flow

In this last test example we consider a water flow problem for wind-driven circulations originally proposed in [27] and widely used to verify the multilayer shallow water models, see for instance [6, 30, 4]. Using the same flow parameters as in these references, we solve the multilayer shallow water equations (2.18) in a squared two-dimensional domain 16 m long filled at 2 m water under a two-dimensional wind force blowing with and angle of 45° and a speed of $w = 20\ m/s$. In our simulations, the Coriolis coefficient $\omega_c = 0$, the viscosity coefficient $\nu = 0.05\ m^2/s$, the friction coefficient $\kappa = 0.00001\ m/s$, the wind stress coefficient $\sigma = 0.0015\ N/m^2$, the water density $\rho = 1025\ kg/m^3$, the air density $\rho_a = 1.2\ kg/m^3$ and the gravity $g = 9.81\ m/s^2$. The bed is assumed to be flat, no-slip boundary conditions are used and we present results for water heights, streamlines and velocity fields at time $t = 50\ s$ using a mesh with 100×100 gridpoints. Figure 4.12 presents the results obtained using 5-layer and 20-layer models. The vorticity plots show that the steady cavity flow within closed streamlines consists of a central inviscid core of nearly constant vorticity with viscous effects confined to thin shear layers near the walls. These plots

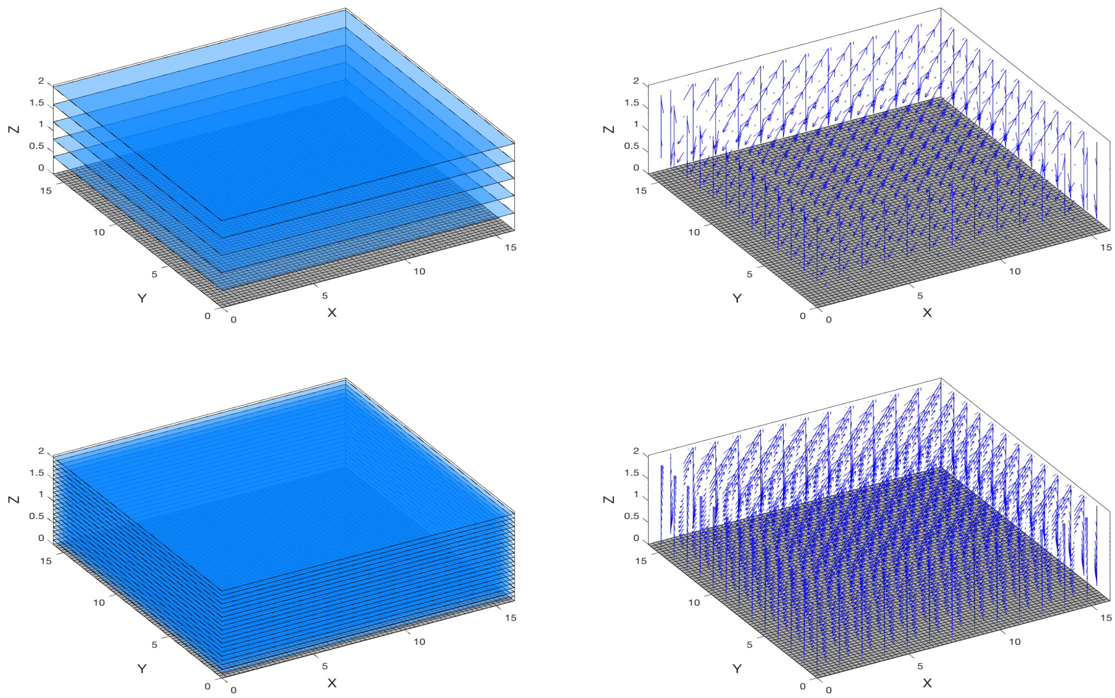

Figure 4.12: Water heights (left) and velocity fields (right) obtained for the wind circulation flow at time $t = 50\ s$ using 5-layer model (top) and 20-layer model (bottom).

also give a clear view of the overall flow pattern and the effect of the number of layers on the structure of the recirculating eddy in the cavity. As expected a recirculation flow is generated in the computational domain and the proposed Eulerian-Lagrangian method resolves the flow features for this test example without relying on the computationally demanding three-dimensional flow models.

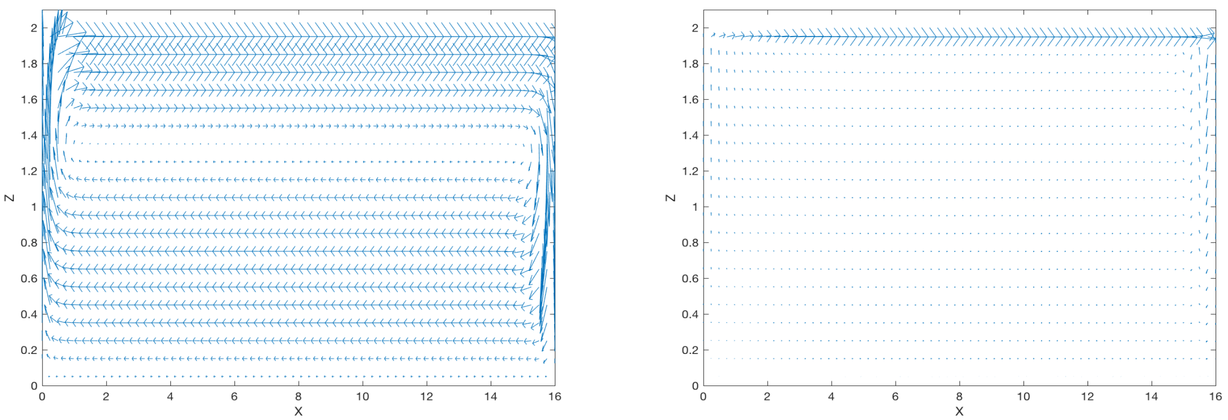

Figure 4.13: Projection of the velocity field in the xz-plane for the wind circulation flow using 20-layer model with viscous terms (left plot) and without viscous terms (right plot) at time $t = 50\ s$.

Next we examine the effect of the coupling terms in the multilayer model (2.1) on the flow structures for this test example. To this end we first solve the equations (2.1) without kinematic eddy viscous terms ($i.e.$ $\mathcal{F}_\alpha^{(u)} = \mathcal{F}_\alpha^{(\nu)} = \mathcal{G}_\alpha^{(u)} = \mathcal{G}_\alpha^{(\nu)} = 0$) and with the viscous terms ($i.e.$ $\mathcal{F}_\alpha^{(\nu)}$, $\mathcal{F}_\alpha^{(u)}$ and $\mathcal{G}_\alpha^{(u)}$, $\mathcal{G}_\alpha^{(\nu)}$ are given

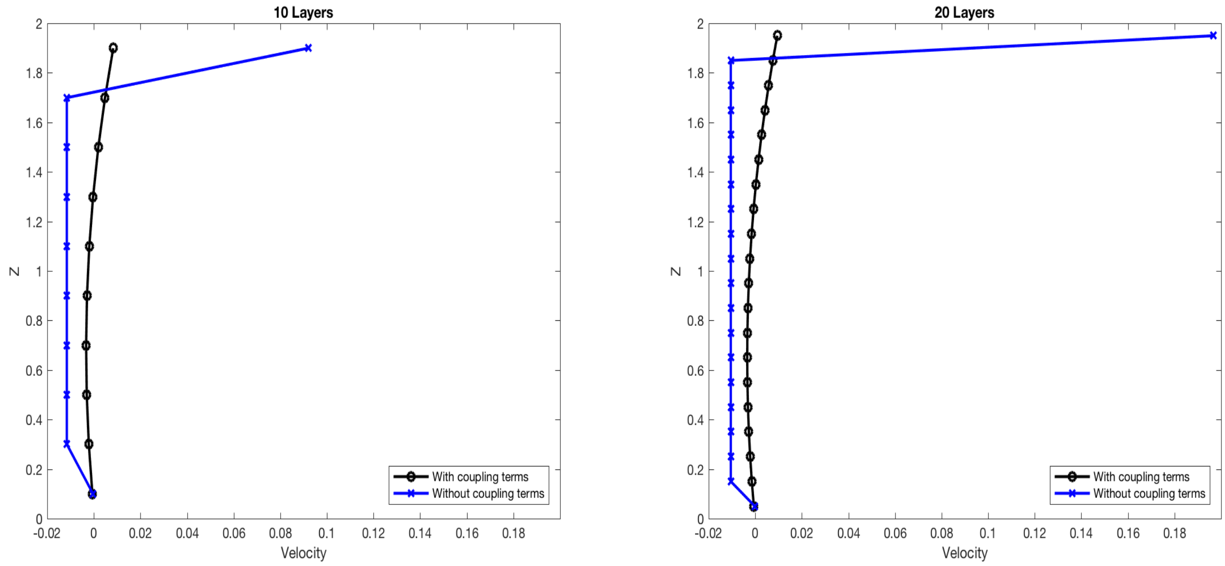

Figure 4.14: Water velocities at the location $(x, y) = (8, 8)$ for the wind circulation flow with and without viscous terms using 10-layer model (left plot) and 20-layer model (right plot) at time $t = 50$ s.

Table 4.1: Values of the x-velocity u at $(x, y) = (8, 8)$ for the wind circulation flow with and without viscous terms using 10-layer model at time $t = 50$ s.

	Layer									
	1	2	3	4	5	6	7	8	9	10
With	-0.0006	-0.0022	-0.0030	-0.0033	-0.0029	-0.0020	-0.0003	0.0019	0.0048	0.0083
Without	-0.0003	-0.0116	-0.0116	-0.0116	-0.0116	-0.0116	-0.0116	-0.0116	-0.0116	0.0920

by (2.6) and (2.14), respectively). The obtained velocity fields in the xz-plane at fixed lateral location $y = 8$ for both cases are shown in Figure 4.13. The effects of the kinematic eddy viscous terms in the multilayer shallow water equations can be clearly seen in these results. Observe the flow patterns at the domain walls and at the bed bottom in the results with and without kinematic eddy viscous terms in Figure 4.13. Accounting for kinematic eddy viscosity in the multilayer model intensifies the recirculation in the flow domain and reproduces a well-developed eddy vortex in the center of the flow domain which is not visible in case of multilayer model without kinematic eddy viscous terms. The center vortex counter-rotating eddies of a much weaker strength develop in the cavity for the simulation without viscous terms $\mathcal{F}_\alpha^{(u)} = \mathcal{F}_\alpha^{(\nu)} = \mathcal{G}_\alpha^{(u)} = \mathcal{G}_\alpha^{(\nu)} = 0$. For a better insight, we present in Figure 4.14 the water velocities at the location $(x = 8, y = 8)$ for 10-layer and 20-layer models with and without viscous terms. The associated values for the velocity in this figures are summarized in Table 4.1. It is clear from these values that simulations without including the viscous terms overestimate the flow velocity whereas, accounting for viscous terms in the simulations predict the corrected flow velocities. The inclusion of these viscous terms is very important for simulation of wind-driven recirculation using the multilayer shallow water equations.

5 Concluding Remarks

A fast and conservative Eulerian-Lagrangian method is proposed for the numerical solution of three-dimensional free-surface flows using two-dimensional multilayer shallow water equations. The governing system consists of a set of two-dimensional hydrostatic multilayer shallow water equations, with mass exchange including eddy viscosity and Coriolis forces on both flat and non-flat beds. Two stages are considered in the procedure to update the solution in time. In the first stage a projection finite volume of the system in local normal and tangential coordinates is used, whereas a method of characteristics is used in the second stage to approximate the numerical fluxes. A second-order splitting operator is also used to deal with the gradient and source terms in the system, and a third-order explicit Runge-Kutta scheme is implemented for the time integration process. This Eulerian-Lagrangian solver employs the modified method of characteristics in a finite volume discretization of the multilayer two-dimensional shallow water system. The method offers the advantage of solving steady three-dimensional free-surface flows over uneven bathymetry while only incurring errors of negligible magnitude. Thus the presented scheme achieves excellent numerical balance between the gradient fluxes and the source terms for this multilayer system. On the other hand, no Riemann problem solvers are needed in the proposed method to compute the numerical fluxes. To examine the performance of the proposed Eulerian-Lagrangian method we solved a wide application of two-dimensional multilayer shallow water equations under contrasting flow conditions. The well-balanced nature of the scheme is presented in the free-surface flow at rest over uneven bathymetry problem. Comparisons to three-dimensional results for incompressible hydrostatic Navier-Stokes equations have also been presented. The results obtained show detailed shock capture with high accuracy in smooth regions. There are also no nonphysical oscillations at the bounds of the shock which often plague high order schemes of this nature. In this study we have used only structured meshes though there is no impediment to the Eulerian-Lagrangian solver being extended to unstructured grids. This and other issues will be the subject of future investigations.

References

[1] M.B. Abbott. *Computational hydraulics: Elements of the theory of free surface flows*. Fearon-Pitman Publishers, 1979.

[2] R. Abgrall and S. Karni. Two-layer shallow water systems: a relaxation approach. *SIAM J. Sci. Comput.*, 31:1603–1627, 2009.

[3] E. Audusse. A multilayer Saint-Venant system: Derivation and numerical validation. *Discrete and Continuous Dynamical Systems, Ser. B.*, 5:189–214, 2005.

[4] E. Audusse, F. Benkhaldoun, S. Sari, M. Seaid, and P. Tassi. A fast finite volume solver for multi-layered shallow water flows with mass exchange. *J. Comput. Physics*, 272:23–45, 2014.

[5] E. Audusse, M. Bristeau, M. Pelanti, and J. Sainte-Marie. Approximation of the hydrostatic Navier–Stokes system for density stratified flows by a multilayer model: kinetic interpretation and numerical solution,. *J. Comput. Phys.*, 230:3453–3478, 2011.

[6] E. Audusse, M.O. Bristeau, B. Perthame, and J. Sainte-Marie. A multilayer Saint-Venant system with mass exchanges for shallow water flows. derivation and numerical validation. *M2AN Math. Model. Numer. Anal.*, 45:169–200, 2011.

[7] F. Benkhaldoun, I. Elmahi, and M. Seaid. A new finite volume method for flux-gradient and source-term balancing in shallow water equations. *Comput. Methods Appl. Mech. Engrg.*, 199:49–52, 2010.

[8] F. Benkhaldoun, S. Sari, and M. Seaid. Projection finite volume method for shallow water flows. *Mathematics and Computers in Simulation*, 118:87–101, 2015.

[9] F. Benkhaldoun and M. Seaid. A simple finite volume method for the shallow water equations. *J. Comp. Applied Math.*, 234:58–72, 2010.

[10] A. Bermudez and M.E. Vázquez-Cendón. Upwind methods for hyperbolic conservation laws with source terms. *Computers & Fluids.*, 23:1049–1071, 1994.

[11] F. Bouchut and T. Morales. An entropy satisfying scheme for two-layer shallow water equations with uncoupled treatment. *M2AN Math. Model. Numer. Anal.*, 42:683–698, 2008.

[12] V. Churuksaeva and A. Starchenko. Mathematical modeling of a river stream based on a shallow water approach. *Procedia Computer Science*, 66:200 – 209, 2015.

[13] R. Codina. Numerical solution of the incompressible Navier–Stokes equations with Coriolis forces based on the discretization of the total time derivative. *J. Comp. Physics.*, 148:467–496, 1999.

[14] D. Dutykh and D. Clamond. Modified shallow water equations for significantly varying seabeds. *Applied Mathematical Modelling*, 40:9767 – 9787, 2016.

[15] E.D. Fernández-Nieto, E. Koné, and Chacón T. A multilayer method for the hydrostatic Navier-Stokes equations: A particular weak solution. *J. Sci. Comput.*, 57:1–30, 2013.

[16] J.F. Gerbeau and B. Perthame. Derivation of viscous Saint-Venant system for laminar shallow water: Numerical validation. *Discrete and Continuous Dynamical Systems, Ser. B.*, 1:89–102, 2001.

[17] J. Gula, V. Zeitlin, and F. Bouchut. Instabilities of buoyancy-driven coastal currents and their nonlinear evolution in the two-layer rotating shallow water model. Part 2. active lower layer. *J. Fluid Mechanics.*, 665:209–237, 2010.

[18] G. Khakimzyanov, D. Dutykh, and Z. Fedotova. Dispersive shallow water wave modelling. Part III: Model derivation on a globally spherical geometry. *Commun. Comput. Phys.*, 23:315–360, 2018.

[19] G. Khakimzyanov, D. Dutykh, Z. Fedotova, and D. Mitsotakis. Dispersive shallow water wave modelling. Part I: Model derivation on a globally flat space. *Commun. Comput. Phys.*, 23:1–29, 2018.

[20] G. Khakimzyanov, D. Dutykh, and O. Gusev. Dispersive shallow water wave modelling. Part IV: Numerical simulation on a globally spherical geometry. *Commun. Comput. Phys.*, 23:361–407, 2018.

[21] G. Khakimzyanov, D. Dutykh, O. Gusev, and N.Y. Shokina. Dispersive shallow water wave modelling. Part II: Numerical simulation on a globally flat space. *Commun. Comput. Phys.*, 23:30–92, 2018.

[22] A.C. Kuo and L.M. Polvani. Nonlinear geostrophic adjustment, cyclone/anticyclone asymmetry, and potential vorticiy rearrangement. *Phys. Fluids.*, 12:1087–1100, 2000.

[23] I. Ozgen, J. Zhao, D. Liang, and R. Hinkelmann. Urban flood modeling using shallow water equations with depth-dependent anisotropic porosity. *Journal of Hydrology*, 541:1165 – 1184, 2016.

[24] A. Robert. A stable numerical integration scheme for the primitive meteorological equations. *Atmos. Ocean.*, 19:35–46, 1981.

[25] D.L. Ropp and J.N. Shadi. Stability of operator splitting methods for systems with indefinite operators: Advection–diffusion reaction systems. *J. Comput. Physics*, 228:3508–3516, 2009.

[26] A. Sattar, H. Jasak, and V. Skuric. Three dimensional modeling of free surface flow and sediment transport with bed deformation using automatic mesh motion. *Environmental Modelling & Software*, 97:303 – 317, 2017.

[27] N.J. Shankar, H.F. Cheon, and S. Sankaranarayanan. Multilevel finite-difference model for three-dimensional hydrodynamic circulation. *Ocean Eng.*, 24:785–816, 1997.

[28] C.W. Shu. Total variation diminishing time discretizations. *SIAM J. Sci. Stat. Comput.*, 9:1073–1084, 1988.

[29] G. Strang. On the construction and comparison of difference schemes. *SIAM J. Numer. Anal.*, 5:506–517, 196.

[30] K.R. Tubbs and F.T.C. Tsai. Multilayer shallow water flow using lattice boltzmann method with high performance computing. *Advances in Water Resources.*, 32:1767–1776, 2009.

[31] J. Yan, X. Deng, A. Korobenko, and Y. Bazilevs. Free-surface flow modeling and simulation of horizontal-axis tidal-stream turbines. *Computers & Fluids*, 158:157 – 166, 2017.

[32] S. Zhao, J. Ovadia, X. Liu, Zhang Y.T., and Q. Nie. Operator splitting implicit integration factor methods for stiff reaction-diffusion-advection systems. *J. Comput. Physics*, 230:5996–6009, 2011.

Durham University
Durham Research Online

Citation on deposit: Sari, S., Rowan, T., Seaid, M., & Benkhaldoun, F. (2020). Simulation of Three-Dimensional Free-SurfaceFlows Using Two-Dimensional Multilayer Shallow Water Equations. Communications in computational physics, 27(5), 1413-1442. https://doi.org/10.4208/cicp.oa-2019-0036

For final citation and metadata, visit Durham Research Online URL:
https://durham-repository.worktribe.com/output/1230108

Copyright statement: This content can be used for non-commercial, personal study.